Episodic crustal extension and compression, characterizing the Late Mesozoic tectonics of East China: Evidence from the Jiaodong Peninsula

Lingtong Meng[1,2], Wei Lin[1,2*]

[1]State Key Laboratory of Lithospheric Evolution, Institute of Geology and Geophysics, Innovation Academy of Earth Science, Chinese Academy of Sciences, Beijing 100029, China

[2]College of Earth and Planetary Sciences, University of Chinese Academy of Sciences, Beijing 100049, China

*corresponding author: Wei Lin (linwei@mail.iggcas.ac.cn)

Key points:

- Polyphase deformations and multiple plutons emplacement were recognized in the Jiaodong Peninsula
- East China experienced a complex tectonic evolution marked by Late Mesozoic intracontinental extension-compression-extension
- Multidisciplinary study improves our understanding on the intracontinental deformations under multi-plate convergences

Abstract

During Late Mesozoic, East China is characterized by widespread magmatism, large-scale thrusting and folding, extensional dome structures, strike-slip faulting and block rotation. It offers an ideal region to understand the episodic intracontinental extension and compression, and associated magmatism under the multi-plate convergences. Based on our structural analyses, magnetic fabrics and gravity modeling, polyphase deformations and magma emplacement have been recognized within the

Que-Kunyu-Yuangezhuang-Sanfo massif in Jiaodong Peninsula, East China. A significant D_1 event with top-to-the-NE high-temperature shearing developed in the northern margin of the massif. Magnetic fabrics and gravity modeling reveal that Late Jurassic plutons display concentric magnetic foliation patterns and NE–SW trending magnetic lineations, built up by several feeder zones at depth. These results support a genetic link between the emplacement of the syn-kinematic plutons (Mag_1) and the regional NE–SW extensional tectonics. In the south of the massif, a lower-temperature top-to-the-SW deformation (D_2) was observed and interpreted as a southeastward thrusting related to the compressional tectonics. The subsequent extensional D_3 event with top-to-the-WNW kinematics corresponds to a NW–SE extensional tectonics. The wedge-shaped Early Cretaceous plutons have sub-horizontal magnetic fabrics and fast cooling rate, implying their emplacement (Mag_2) are controlled by pre-existing fractures in the upper crust. With the pre-existing geochronological results, timing of these tectonic events was discussed. These new data indicate that East China experienced an episodic intracontinental extension and compression during Late Mesozoic. Finally, we proposed that the direction change of the plate convergences caused the Late Mesozoic geodynamic evolution in East China.

Keywords

Intracontinental deformation, Granitic pluton structural analyses, Anisotropy of magnetic susceptibility, Gravity modeling, East China geodynamics

1 Introduction

In the typical collisional or accretionary orogens, the deformation mainly focused on the plate boundaries and nearby, since the continent interior is considered to be rigid. However, the intensive deformation could still be well-developed in the continental interior, even though it is far away from the plate boundaries (*e.g.,* Dickinson & Snyder, 1978; Roure *et al*., 1989; Avouac *et al*., 1993; Chu *et al*., 2012). During Late Mesozoic, East China are surrounded by multi-plate convergences, including the closure of the Mongol-Okhotsk ocean to its north, Izanagi Plate subduction to its east and the collision between the Lhasa and Qiangtang terranes to its west (Maruyama *et al*., 1997; Leier *et al*., 2007; Van der Voo *et al*., 2015). In this scenario, East China is characterized by widespread magmatism, large-scale thrusting and folding, extensional dome structures, strike-slip faulting and block rotation (Dong *et al*., 2015 and references therein). It offers a key area to understand the mechanism of episodic intracontinental extension and compression, and associated magmatism under the multi-plate convergences.

Previous studies focused on the Jurassic–Cretaceous tectonic evolution of the East China suggested (1) two significant episodes of compressional tectonics during Jurassic–earliest Cretaceous (Wong, 1929; Chen, 1998; Davis *et al*., 2001; Darby & Ritts, 2002; Davis *et al*., 2009; Faure *et al*., 2012), (2) subsequent widespread Early Cretaceous extensional tectonics, characterized by numerous extensional basins, metamorphic core complexes (MCC) and syn-kinematic plutons (Davis *et al*., 2002; Ren *et al*., 2002; Meng, 2003; Lin *et al*., 2011; Wang *et al*., 2012; Lin *et al*., 2013a; Liu *et al*., 2013; Zhu *et al*., 2015; Lin & Wei, 2018) and (3) long-term magmatism last from 170-110 Ma with the Late Jurassic (170–150 Ma) and the Early Cretaceous (135–110 Ma) magmatic flare-up (Wu *et al*., 2019). These events have been considered differently by different authors based on regional unconformities, polyphase deformations and magmatism, leading to a broad tectonic framework about the understanding of the Late Mesozoic tectonic evolution of East China. Especially for the Late Jurassic–

earliest Cretaceous tectonics, its timing and kinematics remain hotly debated, and the interplay between structure and magmatism are still poorly constrained (Dong *et al*., 2015). More importantly, the Early Cretaceous crustal extension is considered to be resulted from the “craton destruction”. Foundering, delamination and lithosphere removal were suggested to be the potential mechanism that make “craton destruction” (*e.g.*, Zhu *et al*., 2011; Lin & Wei, 2018; Wu *et al*., 2019), by which the old, thick and refractory Archean lithospheric mantle is replaced by juvenile and fertile lithospheric mantle (Menzies *et al*., 1993; Xu, 2001, among others). The Late Mesozoic tectonic evolution also facilitates to understand the mechanism of “craton destruction”.

To construct the dynamic evolution of the episodic compression and extension, considering the emplacement and exhumation of the massif composed of the granitoids and gneiss is an effective way. Pluton emplacement is usually controlled by internal dynamics and external tectonism (Miller *et al*., 2009; Žák *et al*., 2013, 2015; Paterson *et al*., 2019, among others), and subsequent exhumation of the massif commonly related to regional ductile shear zones (Lin *et al*., 2013a; Rabillard *et al*., 2015; Wei *et al*., 2016; Ji *et al*., 2018a, among others). Hence, the history of the emplacement-exhumation contains significant information on regional tectonics. It also can be determined by the fabric patterns, shapes at depth, and kinematics of major ductile shear zones along the margins.

The eastern margin of East China (*i.e.,* Jiaodong Peninsula) acts as a key area to understand the complex plutonic-tectonic history, because abundant deeper rocks related to the Late Mesozoic deformation are exposed. In this paper, the Que-Kunyu-Yuangezhuang-Sanfo (QKYS) massif located in the central part of the Jiaodong Peninsula (Figure 1) was targeted for the following reasons. Firstly, it comprises Late Jurassic and Early Cretaceous granitic intrusions with their host metamorphic rocks, and experienced polyphase deformation. Secondly, the Late Jurassic and Early Cretaceous plutons emplaced into the middle crustal and upper crustal levels, respectively (Dou *et al*., 2018). Thirdly, the fabric patterns and deep shapes of massif are accessible through the methods of structural analyses, anisotropy of magnetic susceptibility (AMS) and gravity survey. Lastly, the crystallization and cooling ages of the massif are already well-defined before. Accordingly, a multidisciplinary study containing structural analyses, AMS and gravity survey is carried out on the QKYS massif. This study aims to depict the multiple emplacement and exhumation of the massif, to interpret the relationship between magmatism and regional tectonics, to discuss the Late Mesozoic tectonic evolution and possible geodynamics of East China.

2 Geological setting of the Jiaodong Peninsula

The Jiaodong Peninsula, bounded by Tan-Lu fault to the west, is situated in the easternmost part of East China. Tectonically, it can be divided into three units: Jiaobei massif in its northwestern part, Northern Sulu massif in its eastern part and Early Cretaceous Jiaolai Basin containing volcanic and sedimentary rocks to the southwest (Figure 1), and recording the Triassic collision between the South China Block (SCB) and North China Craton (NCC). Even it is famous for the ultra-high pressure (UHP) metamorphic rocks in its eastern part (Wang *et al*., 1993; Ames *et al*., 1996).

From the view of the composition, the Jiaobei massif is considered as a part of NCC and contains three main metamorphic units. From bottom to top of the rock-pile: (1) Neoarchean to Early Paleoproterozoic tonalite-throndhjemite-granodiorite (TTG), gneissic-migmatite, granulite with meta-mafic or amphibolite lenses (Hacker *et al*., 2006; Zhang *et al*., 2014), (2) Paleoproterozoic metamorphic sedimentary rocks including the mica-schists, paragneiss, marble and minor amounts of amphibolite (Wan *et al*., 2006; Tam *et al*., 2011), which experienced 1.8 Ga amphibolite-face metamorphism (Jahn *et al*., 2008), (3) Neoproterozoic weakly or non-metamorphic terrigenous rocks (Li *et al*., 2007).

The Northern Sulu massif mainly consists of migmatite, gneiss, quartzite, marbles and meter-sized blocks of mafic to ultramafic rocks (Fig. 1B; Wang *et al*., 1993). Geochronological study indicates that their protolith age is about 0.8 Ga with some 1.8 Ga ages, suggesting an SCB affinity for the massif (Ames *et al*., 1996; Liu & Liou., 2011). Eclogites are enclosed as blocks within these rocks. In particular, the discovery of coesite as inclusion within the melanosome of migmatite and orthogneiss implies that these rocks experienced a UHP metamorphism (Wang *et al*., 1993; Wallis *et al*., 1997). It is well accepted that the UHP eclogites formed during the deep subduction of the SCB beneath the NCC; the retrograde metamorphism of UHP eclogites and migmatization are associated with the Late Triassic extensional tectonics (Faure *et al*., 2001, 2003a).

Widespread Mesozoic intrusive rocks are exposed in the Jiaodong Peninsula. These intrusions can be divided into four groups according to their age: (1) Late Triassic syenite, (2) Late Jurassic monzogranite, (3) Early Cretaceous porphyritic granitoid and (4) Early to Late Cretaceous mafic-intermediate dykes (Guo *et al*., 2005). The Late Jurassic plutons are derived from the partial melting of a thickened lower crust, while the Cretaceous plutons and dykes are resulted from the removal of the lithospheric mantle, accompanied by the asthenospheric upwelling (Yang *et al*., 2008; Goss *et al*., 2010; Zhang *et al*.,2010). It should be noted that the significant Late Mesozoic deformations are mainly distributed in the margins of the Late Mesozoic plutons with their host rocks (Figure 1; Charles *et al*., 2011a; Xia *et al*., 2016)

3 Structural analysis of the QKYS massif

3.1 Litho-tectonic units of the QKYS massif

As a part of the Jiaobei massif, the NNE–SSW trending QKYS massif is composed of Late Mesozoic plutons and their host metamorphic rocks and experienced significant ductile deformation (Figures 2 and 3), acting as an ideal area to understand the Late Mesozoic tectonic evolution. The western margin of the QKYS massif is a ductile shear zone that separates the massif from the Early Cretaceous volcanic-sedimentary rocks. The Taocun and Mishan faults are considered as its northwestern and eastern boundaries, respectively. To its north and south, the massif is covered by the Cenozoic sediments (Figure 2). It can be divided into four litho-tectonic units: (1) Neoarchean to Early Paleoproterozoic TTG, gneissic-migmatite, granulite with meta-mafic or amphibolite lenses, (2) Paleoproterozoic metamorphic sedimentary rocks including the mica-schists, paragneiss, marble and minor amounts of amphibolite, (3) Late Jurassic Que (Q) and Kunyu (K) plutons composed of medium- to coarse-grained biotite monzogranite, and (4) Early Cretaceous Sanfo (S) and Yuangezhuang (Y) porphyritic granite. In the map scale, the Q and K plutons with irregular shape intruded into the metamorphic rocks. The Q pluton was separated into two parts due to the late sinistral strike-slip movement of the Zhuwu Fault (Figure 2). The S pluton with a NE–SW trending long axis intruded into the K pluton, while the half-elliptical Y pluton emplaced along the margin of Q pluton (Figure 2).

Geochronologically, Neoarchean to Early Paleoproterozoic igneous protoliths, including 2.6–2.5 Ga meta-mafic rocks and 2.7–2.4 Ga TTG, were identified in the south of the massif (Haiyangsuo area), and the metamorphic sedimentary rocks are considered to be deposited at 2.1–1.9 Ga (Liu *et al*., 2017a). The ages of Q and K plutons have a board range of 163–141 Ma yielded by different analytical methods (Figure 4A). The zircons of K and Q plutons are complicated. Most zircons have the inherited core (*e.g.*, Guo *et al*., 2005; Zhao *et al*., 2016) and were disturbed by later thermal event (*e.g.*, Xia *et al*., 2016). During the analysis, the analysis results will be seriously interfered, leading the ages of some zircons older or younger more or less. Hence, we use statistical peak as the crystallization age of these two plutons (Figure 4B) to suppress these uncertainties as much as possible. Meanwhile, most parts of massif have the cooling ages of Early Cretaceous (*i.e.,* 129–120 Ma), while the older cooling ages (219–133 Ma) are presented in the southern part of the massif (Figure 4C). With regards to the S and Y plutons, their zircon U-Pb and biotite $^{40}Ar/^{39}Ar$ ages show an indistinguishable range of 118–113 Ma (Figure 4), implying the Early Cretaceous plutons have an extremely fast cooling rate.

3.2 Bulk Architecture and kinematic analyses

Well-foliated or mylonitic gneiss, schists, marble and amphibolite are exposed among these granitoids. Meanwhile, the deformed granites are mainly exposed in the margins of the Late Jurassic plutons. A clear foliation can be observed in the northern margin of K pluton. The Q pluton is intensively deformed along its western margin to form mylonite. All of these foliations are sub-solidus, characterized by the elongation of recrystallized quartz aggregates with the rotated feldspar porphyroclast (Figure 5A and B). A homogeneous monzogranite type is dominant in K and in the northeast of Q (Figure 5C). Either in their margins or interiors, the S and Y plutons are isotropic with no particular mineral fabric (Figure 5D).

Based on our structural analysis, we suggest that the bulk architecture of QKYS massif is dominated by a Late Mesozoic dome that experienced ductile deformations along its northern, southern and western margins (Figures 2, 3 and 6).

Along the N-margin of K pluton, a solid-state foliation develops, a few hundred meters thick inside the pluton, pointing to the existence of the deformation event. The foliation of the deformed granite mainly dips at moderate to low angle to the N, NE or E, while the mineral lineation is rare (Figure 6A). The gneisses as the host-rock of K pluton are well-foliated to mylonite, with an dominate NW–SE striking foliation close to the N-margin of K (Figure 6B). In these metamorphic rocks, the foliation is parallel to the granite/host-rocks contact, with locally a NE–SW-trending sub-horizontal mineral lineation (Figures 6B and 7A). Along the NE–SW lineation, a top-to-the-NE sense of shear is revealed by sigmoidal feldspar porphyroclasts within the gneiss and foliated granite (Figure 7B and C). Observation of XZ thin sections of the deformed gneiss (*i.e.,* perpendicular to foliation and parallel to the NE–SW mineral lineation), reveals that the sigmoidal feldspar porphyroclasts displaying a top-to-the-NE sense of shear (Figure 7D).

In the south of the massif, the Neoarchean to Early Paleoproterozoic TTG, gneiss with amphibolite lens and Paleoproterozoic metamorphic sedimentary rocks are exposed (Figure 2). These metamorphic rocks are intensively mylonitized with a well-developed sub-horizontal foliation gently dipping to the SW (Figure 6C). Semi-penetrative stretching lineations (Figure 8A) are consistently oriented along a NE–SW trend with a maximum around 65°/10° (Figure 6C). The isoclinal NE–SW trending fold-axes are well developed in the mica-schist (Figure 8B). Along the NE–SW lineation, top-to-the-SW ductile shear criteria are documented by asymmetric felsic lens in the mica-schist (Figure 8C), sigmoidal feldspar porphyroclast within the mylonites (Figure 8D and E), and sigmoidal features observed under the microscope (feldspar porphyroclasts: Figure 8F, and mica fishes: Figure 8G).

In the western boundary of the massif, a decameter to kilometer thick ductile shear zone separates the massif from the overlying Early Cretaceous volcanic and sedimentary rocks, which is split into two parts by brittle sinistral Zhuwu fault (Figure 2). It is sealed by the Early Cretaceous non-foliated Haiyang pluton to its south and covered by late Early Cretaceous sedimentary rocks to its north, respectively (Figure 2). Brittle normal faults overprinting the ductile shear zone control the development of a half-graben basin filled with Early Cretaceous volcanic and sedimentary rocks (Wang *et al*., 2015; Li & Hou, 2018). The mylonitic rocks belonging to the shear zone exhibit pervasive foliations more-or-less parallel to the western margin of the Q pluton. The mylonitic foliations gently dip to the NW, WNW or SW at moderate to low angles (5°–40°), and change to dip to SE or NE away from the west margin (Figures 2 and 6D). The foliated metamorphic rocks observed between the Q and K plutons correspond indeed to the mylonites belonging to the Q pluton, which displays a SE-dipping foliation (Figure 6E). Whatever the dip direction of the foliation, a conspicuous mineral lineation with a dominant WNW–ESE trend and slight plunges (0°–20°) is exhibited on the foliation (Figure 6D and E). The mineral lineation is marked by the preferred orientation of feldspar and quartz aggregates (Figure 9A). At the outcrop and specimen scales, a top-to-the-WNW sense of shear is marked by asymmetric boudins, sigmoidal feldspar porphyroclasts and S-C features (Figure 9B, C and D). In thin sections, a consistent top-to-the-WNW shearing is also documented by sigmoidal porphyroclasts, quartz asymmetric pressure shadows and shear bands (Figure 9E and F).

3.3 Microstructural study in the QKYS massif

3.3.1 Microstructural observation and distribution

Such a study is required to distinguish solid-state microstructures from magmatic microstructures, which has been applied by many researchers and proved to be effective (Bouchez *et al*., 1990; Miller & Paterson, 1994; do Nascimento *et al*., 2004; Xue *et al*., 2017, among others). The specimens were cut into XZ thin section defined by the AMS-framework or tectonic-framework (*i.e.,* parallel to magnetic/ mineral lineation and perpendicular to magnetic/mineral foliation) to be observed under the microscope. According to the criteria suggested by Bouchez *et al*., (1990, 1992), Paterson *et al*., (1998), and Vernon (2000), four types of microstructures are discriminated, including (1) magmatic microstructures, (2) sub-magmatic microstructures, (3) high-temperature solid-state microstructures and (4) low-temperature solid-state microstructures.

Magmatic microstructures. Such microstructures are defined by the absence of solid-sated deformation after magma full-crystallization. Under the microscopic, they display anhedral, medium- to coarse-grained quartz with no obvious preferred orientation and no sub-grains surrounding euhedral feldspars (Figure 10A). Only slight undulose extinction is observed in the quartz, and the feldspars keep straight twin boundaries. The biotite grains are euhedral, mostly isolated in a quartz-feldspar groundmass. And they do not show kinked shapes nor bent boundaries. This type is mainly located in the northeast of Q pluton, and K, S and Y plutons interiors (Figure 11).

Sub-magmatic microstructures. This type is featured by microfractures in plagioclase/K-feldspar crystals filled by quartz (Figure 10B) and the occurrence of the myrmekite (Figure 10C). It results from syn-magmatic deformation at the grain-scale in the presence of a residual melt. This microstructure is occasionally observed in the N-margin of the K pluton (Figure 11).

High-temperature solid-state microstructures. It is characterized by the recrystallized quartz ribbon and rotated feldspar porphyroblasts (Figure 10D). Some plagioclases also show progressive recrystallization to form core-mantle structure. This type is mainly predominant in the N- margin of the K pluton (Figure 11). It is also noted that a continuous transition from magmatic or sub-magmatic microstructures to high-temperature solid-state microstructures is shown from the interior of K pluton to its N-margin.

Low-temperature solid-state microstructures. The most significant feature is the presence of plastic deformation in quartz, marked by undulose extinctions, replacement of primary coarse-grained quartz by recrystallized new grains and shape preferred orientation of these new developed grains (Figure 10E). Biotite displays extensive tearing and kinking. The feldspars mostly maintain their euhedral shape or behavior as rotated porphyroblasts in the mylonite (Figure 10E and F). This type is mainly recognized in the western and south margins of the massif (Figure 11).

3.3.2 Quartz c-axis fabrics

Along the northern, southern and western margins, the foliated to mylonitic rocks are tested for the lattice preferred orientation by using the universal stage method, furtherly to estimate their deformation temperature.

In the northern margin, three samples of foliated granite (KY05, KY09 and KY57) were selected for the analysis of Lattice Preferred Orientation (LPO) of quartz c-axis using the universal stage method. Samples KY09 and KY57 are characterized by point maxima around the stretching lineation (X-axis) and an elongated concentration at the Y-axis (Figure 11). It inferred a combination of prism <c> and prism <a> slip of quartz, pointing to medium- to high- temperature deformation (500–600 °C; Stipp *et al*., 2002). The presence of sub-maxima surrounding the Z-axis (Figure 11) can be explained by the simultaneous presence of basal <a> slip in addition to prism <c> and prism <a>. Asymmetry of these maxima surrounding X-axis unambiguously indicates a top-to-the-NE shearing. The quartz fabric of

KY05 is less clear, with a Z-maximum, a Y-maximum and a subordinate cluster at X-axis, suggesting a combination of basal <a>, prism <a> slip and a subordinate high-temperature prism <c> slip. In conclusion, a medium- to high-temperature condition for the deformation event, likely with a top-to-the-NE sense of shear in the northern margin of the K pluton, can be derived from these c-axis measurements.

Optical measurement with a U-stage of quartz c-axis's LPO helped to estimate the temperature condition of the top-to-the-SW shearing. For this purpose, three samples of mylonitic gneiss (18JD13, 18JD18 and 18JD28) and one mica-schist (18JD29) are chosen. These samples exhibit asymmetric point maxima which are located close to Z, the foliation pole, pointing to the basal <a> slip system of quartz as the dominant slip system. The asymmetrical location of these maxima unambiguously indicates a top-to-the-SW shearing (Figure 11). In addition, samples of 18JD28 and 18JD29 contain sub-maxima in-between Z-axis and Y-axis or close to Y-axis that call to the activity of rhomb <a> slip system (Figure 11). According to the natural and experimental data reviewed in Passchier & Trouw (2005), a low- to medium- temperature condition (~300–400 °C) is responsible for the top-to-the-SW shearing in the south of the massif.

Again, five mylonite samples (QS27, QS30, QS37, QS43 and 18JD125) were chosen along the western margin of the massif (Figure 11). The quartz fabrics of these sample QS27, QS30, QS43 and 18JD125 display the asymmetrical point maxima close to the periphery of the great circle and around the Z-axis, implying the basal <a> slip of quartz at low temperature (*e.g.,* Bouchez, 1977). Several sub-maxima around the Y-axis are also presented in these four samples, corresponding to the rhomb <a> slip at low to medium temperature condition (*e.g.,* Schmid & Casey, 1986, among others). The sample QS37 show two asymmetrical c-axis concentrations around Y, which is attributed to the rhomb <a> slip. Fabric asymmetry also reveals a top-to-the-WNW sense of shear, like that observed in the field. Contrasting the recrystallized quartz (Figure 10E) in the W-margin of the massif with the brittle-ductile behavior of quartz in the S-margin of the massif (Figure 10F), we suggest a slightly higher deformation temperature in the W-margin of the massif. Hence, we give a rough estimation of a low- to medium-temperature condition (~350–450 °C) for the top-to-the-WNW shearing.

4 Anisotropy of magnetic susceptibility (AMS) study

The AMS method, as applied in many studies relative to granitic massifs, offers an effective way to refine their structural elements, particularly among plutons that appear to be isotropic (*e.g.,* Bouchez, 1997; Archanjo *et al*., 2002; Lin *et al*., 2013b; Žák *et al*., 2013, 2015; Wei *et al*., 2014a, among others).

4.1 Sampling and measurement

A total of 111 sampling sites (47 from K pluton, 34 form Q pluton, 18 from S pluton and 12 from Y pluton) were chosen for this study. Except for the southern part of K pluton, where the outcrops are limited in number, the sampling sites are nearly evenly distributed in map view. Each site contains 5 to 8 specimens with regular spacing intervals. They were drilled by portable gasoline drill and were oriented by magnetic compass and solar compass when possible. The specimens were cut into standard specimens 2.2 cm in length and 2.5 cm in diameter.

The AMS measurement of each specimen was performed using an AGICO Kappabridge magnetic susceptometer (MFK1) that works at a low magnetic field at the Institute of Geology and Geophysics, Chinese Academy of Sciences, Beijing, China. The AMS ellipsoid of a given specimen is characterized by three orthogonal principal axes (in orientation and magnitude). For each site, including a group of specimens, the AMS data were processed using Anisoft 4.2 software to acquire the site-average directions and magnitudes of the three principal axes, $K_1 \geq K_2 \geq K_3$ (Jelinek, 1978). The mean magnetic susceptibility (K_m) is equal to their average value ($K_m = (K_1+K_2+K_3)/3$). Two magnetic fabric parameters P_j and T represent the degree of anisotropy and the shape of the AMS ellipsoid, respectively. These parameters are defined by the equations:

$P_j=\{2[(\ln K_1-\ln K_m)^2+(\ln K_2-\ln K_m)^2+(\ln K_3-\ln K_m)^2]\}^{1/2}$ and $T=(2\ln K_2-\ln K_1-\ln K_3)/(\ln K_1-\ln K_3)$ (Jelinek, 1981).

In most rocks, K_1 and K_3 represent the magnetic lineation and the pole to the magnetic foliation, respectively. To define the magnetic carriers, principally ferromagnetic or paramagnetic, and the magnetic grain size of the magnetic carriers, principally pseudo-single domain or multidomain in granites, three complementary measurements are necessary: (1) thermomagnetic curves, (2) isothermal remanent magnetization and (3) hysteresis loops. These measurements were performed at the Institute of Geology and Geophysics, Chinese Academy of Sciences, Beijing, China. Thermomagnetic curves were obtained using a heating apparatus attached to the MFK1 susceptometer. Both isothermal remanent magnetization and hysteresis loop measurements were obtained by using a Micro 3900 Vibrating Sample Magnetometer.

4.2 Magnetic mineralogy

The mean magnetic susceptibility (K_m) of each measured site are presented in Table S1, and the frequency histograms are given in Figure 12. Overall, K_m of S and Y plutons are mostly up to 10^{-2} SI, implying ferromagnetic minerals as the main magnetic susceptibility carriers ($K_m > 5\times10^{-3}$ SI, Hrouda & Kahan, 1991; Bouchez, 1997). The K and Q plutons have K_m ranging from 0.09×10^{-3} SI to 57×10^{-3} SI and 0.036×10^{-3} SI to 16×10^{-3} SI, respectively. In these two plutons, both paramagnetic and ferromagnetic minerals are likely to be AMS carriers; the paramagnetic minerals (iron silicates: biotite and amphibole) become prevailing with a decrease of K_m.

All thermomagnetic experiments (Figure 13A, B and C) display a susceptibility drop at the Curie temperature (~ 580 °C), revealing that iron-rich magnetite is the main susceptibility carrier. The specimens of KY29 and QS22 with low-susceptibility exhibit hyperbolic thermomagnetic curves in the initial part of the curves up to temperatures about 150°C or 250°C, reflecting a significant contribution (>

50%) from paramagnetic minerals (*e.g.,* Trindade *et al*., 1999). The fact that the cooling curve has a higher magnetic susceptibility than that of the heating curve (for example, KY29 in Figure 13A) indicates that the original magnetic phase has been (partly) transformed into magnetite during heating (Bowles *et al*., 2013). At applied magnetic field less than 200 mT, the isothermal remanent magnetization acquisition diagrams (Figure 13D, E and F) display positive correlations between induced magnetization and applied field. At a higher applied field up to 200 mT, induced magnetization of the samples become constant. This observation indicates that our magnetite grains are weakly coercive. The traditional hysteresis ratios M_r/M_s and H_{cr}/H_c are acquired from the experiments of isothermal remanent magnetization and hysteresis loops. The M_r/M_s vs. H_{cr}/H_c plots (Dunlop, 2002) presented in Figure 14 indicate that the magnetic grain-size falls into the range of pseudo-single domain. In fact, these characteristics of magnetic minerals are common in the granites (*e.g.,* Trindade *et al*., 1999; do Nascimento *et al*., 2004, among others).

4.3 AMS fabric parameters

In our case, more than 95% of the measured samples of S and Y plutons have low P_j, less than 1.2. In K pluton, 70% of the P_j values are also less than 1.2 and the remaining 30% of higher values are mainly distributed along the pluton margin and contact with the S pluton (Figure 15A). In the case of Q pluton, 29% of the P_j values exceed 1.2 are presented at its western part where the solid-state deformed rocks are dominated (Figures 11 and 15A). The majority of susceptibility ellipsoids are oblate, materialized by positive T values: 69% in K pluton; 71% in Q pluton; 92% in S, and 99% in Y pluton, suggesting that planer fabrics are better defined than linear ones. There is no positive or negative correlation between P_j and K_m, between T and K_m, or between T and P_j (Figure 15B, C and D). In other words, the P_j, T and K_m values seem to be independent with each other.

4.4 Magnetic foliation and lineation

The tensorial mean orientation of each axis and confidence ellipses, calculated by Anisoft 4.2 software (Jelinek, 1978), are shown on the lower hemisphere equal-area projection (Figure 16). The orientations are considered as well-defined if their confidence level ($\alpha_{95max+}\alpha_{95min}$) is less than 40° (see Table S1). The magnetic foliations (planes normal to K_3) and the lineations (K_1) are represented in map view of Figure 17, along with corresponding orientation diagrams giving sectorial summaries.

The magnetic foliations of K pluton mainly exhibit concentric patterns, thereby, we grouped them into three domains. They dip to NE or W at gentle to moderate angles in domain I, dip to SE or SW with varying angles (25–80°) in domain II and dip inward at moderate to high angles in domain III. The magnetic lineations mainly display shallow plunges (5–20°) with a NE–SW trends in domain I, and ~ENE–WSW trends with varying plunges in domain III. By contrast, scattered lineations with gentle plunging are shown in domain II.

In Q pluton, the AMS orientation data present two distinct fabric patterns. In domain I, the magnetic foliations mainly dip to the NE with varying angles (20°–80°) and the magnetic lineations show variable trends. It worth noting that the magnetic lineations have a consistent gently NE–SW trending in the northeast part of the Q pluton, similar to that in domain I of K pluton. In domain II, the foliations are mainly sub-horizontal, so the foliation poles cluster at the orientation diagram center. The magnetic lineations in domain II display a well-defined NW–SE direction with small angles.

In the S and Y plutons, the magnetic foliations have low outward dips and exhibit a concentric pattern in the map view. The lineations of S pluton consistently plunge shallowly to the NW or SE, so they are distributed along the NW or SE margin of the orientation diagram. Concerning Y pluton, the magnetic lineations have variable orientations with predominant outward plunges.

5 Gravity Survey

Gravity survey applied to numerous studies offer a probable way to reveal the geological features at depth (*e.g.,* Guineberteau *et al*., 1987; Vigneresse, 1990; Vigneresse & Bouchez, 1997; Gébelin *et al*., 2006; Turrillot *et al*., 2011, among others). In our study, the gravity map interpretation and gravity modeling were carried out to characterize the shape of unexposed parts of the QKYS massif.

5.1 Gravity map processing and interpretation

A 1:200000 Bouguer anomaly map of Jiaodong Peninsula was acquired from the Geological Survey of China. In order to extract the long wavelengths of the Bouguer anomaly, a low-pass Butterworth filter with a cutoff wavelength of 150 km was applied on this Bouguer anomaly map. In this map, the regional gravity trends crosscut the lithological boundaries presented on the geological map, implying that the long wavelengths Bouguer anomaly is devoid of the effect of the upper crust (*e.g.,* Wei *et al*., 2014b). The residual gravity anomaly map (Figure 18) obtained through subtraction of the long wavelengths Bouguer anomaly from the original anomaly map mainly reflects the density heterogeneities in the upper crust of the Jiaodong Peninsula.

In residual gravity anomaly map (Figure 18), the iso-gravity trends are nearly parallel to the outcropping plutons' borders, and most of the plutons are represented by negative gravity anomalies. In the QKYS massif itself, no bright contrast appears between the plutons and their country rocks, implying that (1) both the plutons and their country rocks have low densities, (2) low-density rocks are dominant in addition to plutons, and (3) some plutons may extend at depth off their outcropping boundaries. A closer examination shows that the residual Bouguer anomaly of the K pluton is elliptical in-shape with a NE–SW trending long axis. Its overall decreasing gravity gradient toward the west and south indicates that K pluton becomes thinner and narrower in these directions. Three clearly defined first-order negative anomalies are present (i) in the center of K pluton, (ii) south of S pluton and (iii) close to the contact zone between Q and Y plutons, suggesting that deep roots are present in these sectors.

5.2 Constraints for 2D gravity modeling

To obtain a realistic geometry of QKYS massif, we measured the density values of plutons and their host rocks by the double-weighing method. We obtained: (1) 2600 kg/m^3 and 2580 kg/m^3 for the Late Jurassic K and Q biotite monzonitic granite and Early Cretaceous S and Y porphyritic granite, respectively; (2) 2670 kg/m^3 for the Early Cretaceous diorite; (3) 2750 kg/m^3 for Paleoproterozoic meta-sedimentary rocks including the paragneiss, schist, amphibolite and marble; (4) 2630 kg/m^3 for the gneissic migmatite in the north of the massif, and 2720 kg/m^3 for the heavier gneiss to the south of the massif, due to the addition of the meta-mafic lens; and (5) 2550 kg/m^3 for Early Cretaceous volcanic and sedimentary rocks.

Topographic corrections of the residual anomaly map were performed based on the International Gravimetric Bureau database. Based on our field structural analysis, geological map, residual gravity anomaly map and density measurements, we built a gravity model with the "Oasis montaj" platform of Geosoft (www.geosoft.com). The density of undifferentiated upper crust was chosen as 2740 kg/m^3, according to the Crust 1.0 model of Laske *et al.* (2013). All layers were set to be nearly flat and extend at infinity to avoid the edge effects. Finally, each unit in the profiles was considered to have a constant density, appropriate to obtain the best match between measured and calculated gravity values.

5.3 Gravity profiles

Five NE–SW trending and six NW–SE trending modeled gravity profiles (Figure 19) crosscutting all litho-tectonic units in the study area, allow us to characterize the shape of QKYS massif at depth. According to these gravity profiles, several features can be outlined. The metamorphic formations (gneissic migmatite and meta-sedimentary rocks) that surround the plutons have a thickness of around 5 km. The K and Q plutons are rather batholithic with considerable thickness variations. In the NE–SW trending profiles, these two plutons count up to 3 deepest roots deeper than ~6 km (Figure 19

A–E), and in-between these roots, their thickness is 2–3 km. In the NW–SE trending profiles (Figure 19 F–K), the Q pluton has a constant thickness of 2 to 4 km with no obvious deeper root. Also, the K pluton displays a constant thickness of 2–4 km with no obvious root (Figure 19 F, J and K) or a significant deeper root up to ~6 km (Figure 19 G, H and I) in the NW–SE trending profiles. Accordingly, we argued that the K and Q plutons are made of several deeper roots arranged along NE–SW trending. Concerning the S and Y plutons, both the NE–SW trending profiles and the NW–SE trending profiles reveal that they have a single ~5 km-deep root (Figure 19). The typical wedge-shaped sections with steep walls, steepening with depth, are shown in the profiles which are perpendicular to elongation of the Y and S plutons (Figure 19E, I, J and K). Profiles H to K show that the top of Q pluton is covered by 1 to 2 km-thick Early Cretaceous volcanic and sedimentary rocks. The contact between the Q pluton and the Early Cretaceous volcanic and sedimentary rock is arch-shaped and becomes steep at depth (Figure 19I, J and K).

6 Discussion

6.1 Origins of the magnetic fabrics

In our case, paramagnetic and ferromagnetic minerals (*i.e.,* biotite, amphibole and magnetite) act as the main AMS carriers; their preferred orientations are attributed to the magnetic fabrics. The mesoscopic foliation and lineation are also oriented by these paramagnetic minerals, which are correspond well to the magnetic foliation and lineation (Figures 2 and 17). Our AMS study identifies two groups of magnetic fabrics in the Late Jurassic Q and K plutons. The first group is composed of concentric magnetic foliations, mainly distributed in the domain I of Q pluton and the domains I, II and III of K pluton. Although the magnetic lineations are variable in the domain I of Q pluton and II of K pluton, predominate (E)NE–(W)SW ones are presented in the domains I and III of K pluton. They also are parallel to the mineral lineation of the high-temperature deformation in the N-margin of the K pluton. Granite samples of this group are featured by the magmatic, sub-magmatic or high-temperature solid-state microstructures (Figure 11). Combing with the geometric relations of plutons and their host rocks (*c.f.* section 3), we suggest the magnetic fabrics of this group acquired during the late stage of magma crystallization, recording syn-emplacement increments of regional tectonic strain (*e.g.,* Žák *et al*., 2015; Paterson *et al*., 2019). The second group is mainly located in the domain II of Q pluton in which the granites have flat magnetic foliations and NW–SE magnetic lineation (Figure 17). It also has low-temperature solid-state microstructures (Figure 11) that correlate well with the higher P_j values (Figure 15A). As a consequence, the magnetic fabrics of second group, which are corresponded to the mylonitic foliations and lineations observed in the western margin of Q pluton, naturally considered to be acquired during the solid-state deformation (*e.g.,* Lin *et al*., 2013b).

The S and Y plutons show typical features of isotropic granitoids with magmatic microstructures, low P_j, and no sub-solidus recrystallization. Together with an extremely fast cooling rate they have, we argued that their magnetic fabrics are devoid of the influence of regional tectonics (*e.g.,* Paterson *et al*., 1998; Yoshinobu *et al*., 1998). In other words, their magnetic fabrics developed during magma crystallization without the contribution of syn- or post-emplacement tectonics.

6.2 Polyphase deformation and multiple pluton emplacement

In our case, several lines of evidence support the polyphase deformation phases rather than a single tectonic event to form the QKYS massif. Firstly, the magnetic foliations of K pluton (*i.e.,* domain II and domain III) decoupled with the foliations of the country rocks in the center and south parts of the massif (Figures 2, 17 and 20). Generally, such geometry cannot be attributed to a single deformation event (*e.g.,* Paterson *et al.,* 2019). Secondly, the typical metamorphic core complex or extensional dome is exhumed through a major ductile shear zone (detachment fault) with the constant lineation direction and kinematics (Davis, 1983; Yin, 2004). Also, there is no case of metamorphic core complexes that is featured by perpendicular lineations with related kinematics along its each side documented in East China (Lin & Wei, 2018). Thirdly, different deformation temperatures determine that these tectonic events occur at different crustal levels, among which the top-to-the-NE shearing is high-temperature, and top-to-the-SW shearing and top-to-the-WNW shearing are low-temperature. Fourthly, the geochronological works also reveal these deformation phases have different timing. Considering these deformations last from Late Jurassic to Early Cretaceous (see the sections of 6.2.1 to 6.2.3), a single tectonic regime (extension or compression) accounting for these events should be unhopeful. This the reason that most geologists interpreted the Late Jurassic compressional tectonics and Early Cretaceous extensional tectonics developed in East China (Davis *et al*., 2001; Faure *et al*., 2012; Lin *et al*., 2013a, 2013b). Based on the geometry of the QKYS massif and related kinematics, even the geochronology and temperature of the deformation, the polyphase deformation is reasonable for understanding the tectonic evolution in the research area.

6.2.1 D_1 deformation coeval with the emplacement of the Late Jurassic plutons (Mag_1)

Along the northern margin of the K pluton, the foliations are parallel between the country rocks (orthogneiss) and granitic rocks. NE–SW mineral lineations are developed on both of them with the similar top-to-the-NE kinematics (Figure 20). A continuous transition from magmatic or sub-magmatic microstructures in the internal part to high-temperature solid-state microstructures along the pluton margin (Figure 11) argue for that the K pluton expressed a feature of the syn-kinematic emplacement. The crystallization age of K pluton (*i.e.,* 153 Ma, Figure 4B) therefore could be considered as the age constraint for the first-stage deformation (*i.e.,* D_1 event).

According to Dou *et al*. (2018), the late Jurassic plutons emplaced at pressures of ~4 kb corresponding to crustal depths of ~15 km. If we take this result into our consideration, our gravity model indicates that it extended down to > 20 km during the D_1 event (roots at -6 km). At the depth, the K and Q plutons are built by several deep roots arranged along NE–SW trending and these deep roots are often considered as the feeder zones of magma (*e.g.*, Améglio *et al*., 1997). The centers of the concentric patterns of the magnetic foliations match well with the feeder zones (Figures 17, 19 and 20), implying the magma inflation above the feeder zones (*e.g.,* Ji *et al*, 2018). Together with the top-to-the-NE kinematics, normal sense of the movement, we argued that the Late Jurassic K and Q plutons emplaced at an extensional setting. In such a tectonic scenario (Figure 21A), the magma emplaced through several feeder zones (*e.g.,* Vigneresse, 1995). When the magma approached the middle crustal level (c.a. 15 km), it laterally expanded along the extensional direction (NE–SW-trending) and crystallized to form the concentric magnetic foliations of K plutons and NE-dipping magnetic foliations of Q pluton (Figure 17). Nearly coeval with the magma crystallization, a high-temperature D_1 ductile shear zone developed along the northern margin of the K pluton due to strain location (Figure 21A). Also, the significant (E)NE–(W)SW-trending magnetic lineations are presented in the north part and south part of K pluton (*i.e.,* domains I and III), recording the syn-magmatic strain. When move to the interior of plutons, the strain decreases, leading the scattered magnetic lineations in the domain II of the K pluton and domain I of the Q pluton (Figure 17).

6.2.2 latest Jurassic to earliest Cretaceous compressional D_2 event

In the south of the QKYS massif, the ductile shear zone displays a gentle SW dipping foliation, NE–SW stretching lineation, and top-to-the-SW kinematics under ~300–400 °C (the low- to medium) temperature condition (Figures 11 and 20). Because later high-temperature deformation can easily erase the earlier low-temperature deformation, we suggest this event should occur later than the high-temperature D_1 deformation and name it D_2 event. The deformation temperature (300–400 °C) of D_2 event is slightly higher than the biotite closure temperature (c.a. 300 °C), and much lower than that of amphibole (c.a. 550 °C). Hence, the biotite $^{40}Ar/^{39}Ar$ age (135–133 Ma) of the gneiss and amphibolite in the south of the massif (Figure 4C) is considered as the lower limit of the timing of D_2. Accordingly, it is reasonable to constrain the timing of the D_2 event between the 135–133 Ma and D_1, *i.e.,* the latest

Jurassic to earliest Cretaceous.

The D_2 event with a top-to-the-SW shearing on gentle SW-dipping shear plane seems to be a plausible normal movement. However, if we take into the geometry of the domal structure related to the massif exhumation (see section 6.2.3), the D_2 architecture should dip to the NE gently (Figure 21B and C). Accordingly, we prefer to considering the D_2 event as a curved SW-ward thrusting that juxtaposed the Neoarchean gneiss over the Paleoproterozoic meta-sedimentary rocks rather than SW-ward normal faulting. Meanwhile, it is striking that either the timing (153–135 Ma) or kinematics (top-to-the-SW) of D_2 events can be comparable with the SW-directed ductile thrusting documented in East China (Lin *et al*., 2013a; Zhu *et al*., 2015). Therefore, we interpret it as a compressional event from the view of geometry, kinematics, age and regional understanding (Figure 21B).

6.2.3 Early Cretaceous extensional D_3 event

Along the western margin of the massif, the flat-lying ductile shear zone with the top-to-the-WNW kinematics separates the Late Jurassic Q pluton and its host rocks from the Early Cretaceous non-metamorphic volcanic and sedimentary rocks (Figure 20). It is interpreted as a detachment fault with normal kinematics leading the QKYS massif exhumated, pointing to an extensional structure. This event also reset the magnetic fabrics of the Q pluton to form the flat magnetic foliations with NW–SE-trending magnetic lineations in its domain II (Figure 17). Two muscovite and five biotite samples from the mylonitic granite along the detachment fault yielded $^{40}Ar/^{39}Ar$ ages of 128–126 Ma (Wu, 2014) and 124–120 Ma (Li *et al*., 2006; Zhang *et al*., 2007; Wu, 2014), respectively (Figure 4C). Considering its deformation temperature between the closure temperature of muscovite (450 °C) and biotite (300 °C), the true age of the detachment fault along the western margin of the Q pluton is about 126 to 124 Ma, *i.e.,* Early Cretaceous. Hence, this event took place after the D_2 event and named it the D_3 event.

Comparable to the typical Cordilleran-type MCC in North American (Davis, 1983), the exhumation process of the QKYS massif was expressed via rolling hinge structure (Wernicke & Axen, 1988). Our gravity modeling reveals the flat-lying detachment fault becomes steeper at depth (Figure 19), likely corresponding to the rolling-hinge structure in which the flat-lying detachment fault was rotated from an initial high angle fault (Axen *et al*., 1995). Rolled around the hinge of the detachment fault, the footwall rocks were progressively exhumed to reach the shallow level (*e.g.,* Ratschbacher *et al*., 2000; Yin, 2004). Hence, the Q pluton immediately below the detachment fault has a younger cooling age than the K pluton that is far away from the detachment fault (Figure 4C). With the exhumation of the massif, the thrust fault related to D_2 is curved to form the SW-dipping foliations in its south part (Figure 21C, NE–SW trending).

6.2.4 Emplacement of Early Cretaceous plutons (Mag_2)

The Early Cretaceous S and Y plutons display wedge-like shape with a single feeder zone in the gravity profiles (Figure 19), implying they emplaced through a single sub-vertical anisotropy zone or as a diapir (*e.g.,* Guineberteau *et al*., 1987; Améglio *et al*., 1997; Kratinová *et al*., 2006). However, the thermomechanical modeling study indicated that the magma ascent through a diapir is prone to stop at the middle to lower crust (Cao *et al*., 2016). Since the S and Y plutons emplaced at a pressure of ~1.8–2.1 kbar, corresponding to crustal depths of ~5.4–6.3 km (Dou *et al*., 2018), the model of diapir has been excluded. Alternatively, we proposed that the sub-vertical anisotropy zone in their host rocks serve as a preferential channel (Figure 21D). As discussed above, the study area has undergone long polyphase deformation during Late Mesozoic. Hence, pre-existing structures, that are generally fractures developed in the upper crust is envisaged to control the emplacement of the S and Y plutons (*e.g.,* Liu *et al*., 2018). Meanwhile, their gentle magnetic foliations represent the sub-horizontal roof at the top of the wedge-shaped pluton.

Another two Early Cretaceous plutons (*i.e.,* 118 Ma Haiyang and 108 Ma Weideshan pluton in Figure 1) have been documented in the Jiaodong Peninsula (Charles *et al*., 2011). These two porphyritic granodiorites share common features like the S and Y plutons, namely (1) typical isotropic textures without obvious solid-state deformation, (2) sub-horizontal and dipping outward magnetic foliation with scattered gentle magnetic lineation, and (3) a fast cooling rate revealed by the zircon U-Pb and biotite $^{40}Ar/^{39}Ar$ ages. Accordingly, isotropic pluton emplacement, devoid of the influence of regional tectonics and controlled by pre-existing structures, may prevail during the 118–108 Ma period in the Jiaodong Peninsula.

6.3 Late Mesozoic episodic extension and compression

In the QKYS massif, polyphase ductile deformation (D_1, D_2 and D_3) and multiple magmatism (Mag_1 and Mag_2), have been recognized. It provides a window to understand the Late Mesozoic tectonic evolution at deeper levels in East China (Figure 22).

Our structural analyses, AMS and gravity modeling show the evidence for the Late Jurassic extensional D_1 event, accompanying the syn-kinematic magmatism (Mag_1). Accordingly, it supports the view of a significant episode of extensional tectonics during Late Jurassic (*i.e.,* 165–150 Ma). In this extensional period, magmatism, volcanism and basins are also widespread (Figure 22A), earlier than the latest Jurassic–earliest Cretaceous folding and thrusting (*e.g.,* Faure *et al*., 2012; Dong *et al*., 2015; Guo *et al*., 2018). Furthermore, our study points to a Late Jurassic NE–SW extension with the top-to-the-NE kinematics.

A significant “magma gap” of 150–135 Ma (J_3–K_1), between two periods of Late Jurassic and Early Cretaceous magmatic flare-up events, is consistent with the J_3–K_1 compressional tectonics (Li, 2000; Wu *et al*., 2019; Li *et al*., 2020). Several lines of evidence, including the regional unconformity, thrust-controlled basin and E–W-trending fold and thrust structures also indicate a NE–SW compressional tectonics during the latest Jurassic–earliest Cretaceous (Wong *et al*., 1929, among others). A representative southward thrusting called Gubeikou fault is dated between148 and 132 Ma in the Yanshan area (Davis *et al*., 2001). Late Triassic or pre-middle Jurassic polyphase deformations have been recognized in the Lingyuan-Qinglong area (Davis *et al*., 2009), and He *et al*., (1998) considered that the SE-directed thrusting took place in Latest Jurassic. In the Liaodong Peninsula, a J_3–K_1 SE-directed thrusting also has been documented (Qiu *et al*., 2018).Even though the thrust-fold structures at shallower levels are characterized by variable thrusting direction, the ductile deformation events developed in the Sihetang, Yiwulüshan and Jiaodong Peninsula (Davis *et al*., 2001; Lin *et al*., 2013a; Zhu *et al*., 2015; D_2 event in this study) point to a consistent top-to-the-SW kinematics at the deeper levels (a summary in the Figure 22B).

The recognition of the D_3 event suggests the study area was subjected to the intense WNW-ESE extension. Previous studies also documented that several Early Cretaceous extensional structures (Figure 22C), including MCCs, magmatic domes, syn-kinematic plutons and detachment fault, are well-developed in the East China (Davis *et al*., 2002, among others). These extensional structures share common features such as a conspicuous NW–SE mineral lineation with either top-to-the-NW or top-to-the-SE kinematics, and supra-detachment basins (Lin & Wei, 2018 and references therein). The dating of syn-kinematic minerals has constrained that these structures occurred at 130–115 Ma, in agreement with the timing of the D_3 event of QKYS massif (Wang *et al*., 2012; Zhu *et al*., 2015; Lin & Wei, 2018 and references therein). In this period, several extensional basins, intensive magmatism and mineralization likewise occurred in East China, which are associated with the extensional tectonics (Ren *et al*., 2002; Meng, 2003). Following the Early Cretaceous extensional tectonics, we deduced that the upper crust becomes highly fractured to provide the channels for Early Cretaceous magma ascent (Mag_2 event). The magnetotelluric profile also supports this hypothesis (Zhang *et al*., 2018).

6.4 Geodynamic Implications

Multiple plates convergences, including the closure of the Mongol-Okhotsk ocean, Izanagi Plate subduction and the collision between the Lhasa and Qiangtang terranes, took place surrounding East China during the Jurassic–Cretaceous (Maruyama *et al*., 1997; Leier *et al*., 2007; Dong *et al*., 2015; Van der Voo *et al*., 2015; Ma *et al.*, 2017). Evaluating the role of every active plate boundary is critical to understand the geodynamics of the Late Mesozoic episodic intracontinental extension and compression. Given either the Late Mesozoic compressional or extensional structures were mostly in the eastern and northern part of East China (Figure 22), a logical dynamic interpretation is the far-away effect of the Izanagi Plate subduction and the closure of the Mongol-Okhotsk ocean (*e.g.,* Davis *et al*., 2001; Zhu *et al*., 2011). Recently, Wu *et al*., (2019) proposed the Izanagi Plate initiated with steep subduction at 200–160 Ma. We thus considered that it has a continuous effect on East China to cause the Late Jurassic (165–150 Ma) extensional tectonics. Late Jurassic Izanagi Plate subduction with a NE direction (Maruyama *et al*., 1997) is also consistent with the NE–SW-trending stretching orientation (Figure 22A). Subsequent counterclockwise change of the subduction direction of the Izanagi Plate (Maruyama *et al.*, 1997), coeval with the convergent tectonism of closure of the Mongol-Okhotsk ocean (Van der Voo *et al.*, 2015) is likely to account for the latest Jurassic to earliest Cretaceous compressional tectonics (Figure 22B). Besides, the change of the subduction angle at this period may another significant reason for the compressional tectonics (Wu *et al*., 2019; Zhang *et al*., 2020).

The rapid change from the latest Jurassic to earliest Cretaceous crustal compression to Early Cretaceous crustal extension favors that a previous thickened crust acts as one of the principal causes for the intense crustal extension. The numerical modeling also points to that the thickened continental crust facilitates the decoupling between the upper crust and the lower crust (Buck, 1991; Burvo, 2010), leading to the intensive extension (Gueydan *et al.*, 2008; Brun *et al.*, 2018). Furthermore, the model of lithosphere foundering is speculated to be a significant geodynamic mechanism that resulted in the loss of the lithospheric root beneath the NCC (Lin & Wei, 2018), through which the continental crust and lithospheric mantle are highly decoupled. Subsequent asthenosphere upwelling led a high mantle heat flux able to weaken the middle-lower crust, favoring the middle-lower crustal rocks prone to feed the exhuming dome (Brun *et al*., 2018). In the plate tectonic framework (Figure 22C), the Early Cretaceous NW-directed subduction of the Izanagi Plate and its subsequent roll-back enhanced the lithosphere foundering, causing the large-scale crustal extension during the Early Cretaceous.

7 Conclusions

To understand episodic intracontinental extension and compression, the QKYS massif in East China provides an excellent case as it experienced polyphase magmatism and deformation events. Based on our structural analyses, AMS study and gravity modeling, three successive deformation events (D_1, D_2 and D_3) and two periods of magmatism (Mag_1 and Mag_2) have been recognized in the massif, controlling its domal architecture and kinematics. The Late Jurassic D_1 event is characterized by the high-temperature deformation with top-to-the-NE normal kinematics, formed at the NE–SW extensional tectonics. In such a tectonic scenario, the syn-kinematic pluton (Mag_1) has concentric magnetic foliations and NE–SW magnetic lineations, built up by several feeder zones at depth. The latest Jurassic to earliest Cretaceous D_2 event with top-to-the-SW kinematics is interpreted to be a low-temperature ductile thrusting in response to the NE–SW compressional tectonics. The D_3 event is featured by a low-temperature rolling-hinge structure with top-to-the-WNW kinematics, which is related to the Early Cretaceous NW–SE extensional tectonics. This event also reset the magnetic fabrics of the Late Jurassic pluton to form flat magnetic foliation and NW–SE-trending magnetic lineation. Finally, the highly fractured upper crust is considered to provide the channels for the Early Cretaceous magma ascent (Mag_2 event).

These new results allow us to construct a comprehensive tectonic evolution with distinct tectonism from NE–SW extension to NE–SW compression, then to NW–SE extension during the Late Mesozoic. A model of Izanagi Plate subduction, coeval with the closure of the Mongol-Okhotsk ocean, can explain the Late Mesozoic dynamic evolution of East China. Particularly, the change of subduction orientation and angle resulted in the episodic extension and compression. Furthermore, this new evolution model indicates that both the previously thickened crust and lithospheric foundering may play significant roles in the Early Cretaceous “craton destruction”.

Acknowledgements

We thank the Editor in Chief Prof. Laurent Jolivet, Associate Editor, Prof. Jiří Žák and Prof. Jean-luc Bouchez for their constructive comments and suggestions that are helpful to improve the manuscript. This study was funded by the Chinese Ministry of Science and Technology (2016YFC0600102 and 2016YFC0600401), and the National Natural Science Foundation of China (91855212, 91755205, and 41472193). The supporting information of the AMS results (Table S1) can be found in https://doi.org/10.6084/m9.figshare.11313335.v5.

References

Ames, L., Zhou, G. & Xiong, B., 1996. Geochronology and geochemistry of ultrahigh-pressure metamorphism with implications for collision of the Sino–Korean and Yangtze Cratons, Central China. *Tectonics, 15*, 472–489. https://doi.org/10.1029/95tc02552

Améglio, L., Vigneresse, J. L., & Bouchez, J. L. (1997). Granite pluton geometry and emplacement mode inferred from combined fabric and gravity data. In J. L. Bouchez, D. H. W. Hutton, & W. E. Stephens (Eds.), Granite: From segregation of melt to emplacement fabrics (pp. 199–214). Paris: Springer Science & Business Media. https://doi.org/10.1007/978-94-017-1717-5_6

Archanjo, C. J., Trindade, R. I. F., Bouchez, J. L., & Ernesto, M. (2002). Granite fabrics and regional-scale strain partitioning in the Seridó belt (Borborema Province, NE Brazil). *Tectonics, 21*(1), 1003. https://doi.org/10.1029/2000tc001269

Avouac, J. P., Tapponnier, P., Bai, M., You, H., & Wang, G. (1993). Active thrusting and folding along the Northern Tien Shan and late Cenozoic rotation of the Tarim relative to Dzungaria and Kazakhstan. *Journal of Geophysical Research 98* (B4), 6755–6804. https://doi.org/10.1029/92jb01963

Axen, G. J., Bartley, J. M., & Selverstone, J. (1995). Structural expression of a rolling hinge in the footwall of the Brenner Line normal fault, eastern Alps. *Tectonics, 14*(6), 1380–1392. https://doi.org/10.1029/95tc02406

Bouchez, J. L. (1977). Plastic deformation of quartzites at low temperature in an area of natural strain gradient. *Tectonophysics, 39*(1-3), 25–50. https://doi.org/10.1016/0040-1951(77)90086-5

Bouchez, J. L., Gérard G, Djouadi, T., & Rochette, P. (1990). Microstructure and magnetic susceptibility applied to emplacement kinematics of granites: the example of the Foix pluton (French Pyrenees). *Tectonophysics, 184*(2), 157–171.

https://doi.org/10.1016/0040-1951(90)90051-9

Bouchez, J. L., Delas, C., Gleizes, G., Nédélec, A., & Cuney, M. (1992). Submagmatic microfractures in granites. *Geology, 20*(1), 35–38. https://doi.org/10.1130/0091-7613(1992)020<0035:smig>2.3.co;2

Bouchez, J. L. (1997). Granite is never isotropic: An introduction to AMS studies of granitic rocks. In Bouchez, J. L., Hutton, D. H. W., & Strphens, W. E. (Eds.), Granite: From Segregation of Melt to Emplacement Fabrics (pp. 95–112). Paris: Springer Science & Business Media. https://doi.org/10.1007/978-94-017-1717-5_6

Bowles, J. A., Jackson, M. J., Berquó, T. S., Sølheid, P. A., & Gee, J. S. (2013). Inferred time- and temperature-dependent cation ordering in natural titanomagnetites. *Nature Communications, 4*(1). https://doi.org/10.1038/ncomms2938

Brun, J. P., Sokoutis, D., Tirel, C., Gueydan, F., Driessche, J. V. D., & Beslier, M. O. (2018). Crustal versus mantle core complexes. *Tectonophysics*, 746(30), 22–45. https://doi.org/10.1016/j.tecto.2017.09.017

Buck, W. R. (1991). Modes of continental lithospheric extension. *Journal of Geophysical Research: Solid Earth, 96*(B12), 20161–20178. https://doi.org/10.1029/91jb01485

Burov, E. B. (2010). The equivalent elastic thickness (T_e), seismicity and the long-term rheology of continental lithosphere: Time to burn-out “crème brûlée”? Insights from large-scale geodynamic modeling. *Tectonophysics, 484*, 4–26. https://doi.org/10.1016/j.tecto.2009.06.013

Cao, W., B. J. P. Kaus, and S. Paterson (2016), Intrusion of granitic magma into the continental crust facilitated by magma pulsing and dike-diapir interactions: Numerical simulations. *Tectonics, 35*, 1575–1594, doi:10.1002/2015TC004076.

Charles, N., Chen, Y., Augier, R., Gumiaux, C., Lin, W., Faure, M., et al. (2011b). Palaeomagnetic constraints from granodioritic plutons (Jiaodong Peninsula): new insights on Late Mesozoic continental extension in eastern Asia. *Physics of the Earth and Planetary Interiors 187*, 276–291. https://doi.org/10.1016/j.pepi.2011.05.006

Charles, N., Gumiaux, C., Augier, R., Chen, Y., Zhu, R. X., & Lin, W. (2011a). Metamorphic core complex vs. synkinematic pluton in continental extension setting: Insights from key structures (Shandong Province, eastern China). *Journal of Asian Earth Sciences, 40*(1), 261–278. https://doi.org/10.1016/j.jseaes.2010.07.006

Chen, A. (1998). Geometric and kinematic evolution of basement-cored structure: intraplate orogenesis within the Yanshan Orogen, North China. *Tectonophysics 292*, 17–42. https://doi.org/10.1016/S0040-1951(98)00062-6

Chen, W., Harrison, T. M., Heizler, M.T., Liu, R., Ma, B. & Li, J., (1992). The cooling history of melange zone in north Jiangsu–south Shandong region: evidence from multiple diffusion domain ^{40}Ar-^{39}Ar thermal geochronology. *Acta Petrologica Sinica, 8,* 1–17. (in Chinese with English abstract)

Chu, Y., Faure, M., Lin, W., & Wang, Q. (2012). Early Mesozoic tectonics of the South China block: insights from the Xuefengshan intracontinental orogen. *Journal of Asian Earth Sciences, 61*, 199–220. https://doi.org/10.1016/j.jseaes.2012.09.029

Darby, B. J., & Ritts, B. D. (2002). Mesozoic contractional deformation in the middle of the Asian tectonic collage: the intraplate western Ordos fold–thrust belt, China. *Earth and Planetary Science Letters, 205*(1), 13–24. https://doi.org/10.1016/S0012-821X(02)01026-9

Davis, G. H. (1983). Shear-zone model for the origin of metamorphic core complexes. Geology, 11(6), 342. https://doi.org/10.1130/0091-7613(1983)11<342:smftoo>2.0.co;2

Davis, G. A., Darby, B. J., Zheng, Y., & Spell, T. L. (2002). Geometric and temporal evolution of an extensional detachment fault, Hohhot metamorphic core complex, inner Mongolia, China. *Geology*, *30*(11), 1003–1006. https://doi.org/10.1130/0091-7613(2002)030<1003:GATEOA>2.0.CO;2

Davis, G. A., Meng, J., Cao, W., & Xingqiang, D. U. (2009). Triassic and Jurassic tectonics in the eastern Yanshan belt, North China: insights from the controversial Dengzhangzi formation and its neighboring units. *Earth Science Frontiers*, *16*(3), 69–86. https://doi.org/10.1016/S1872-5791(08)60090-1

Davis, G. A., Zheng, Y. D., Wang, C., Darby, B. J., Zhang, C. H., & Gehrels, G. (2001). Mesozoic tectonic evolution of the Yanshan fold and thrust belt, with emphasis on Hebei and Liaoning provinces, northern China. *Geological Society of America Memoirs*, *194*, 171–194. https://doi.org/10.1130/0-8137-1194-0.171

Dickinson, W. R., & Snyder, W. S. (1978). Plate tectonics of the Laramide orogeny. In: Matthews Ili, V (Ed.), Laramide Folding Associated with Basement Block Faulting in the Western United States. *Geological Society of America Memoir*, *151*, 55–366.

do Nascimento, H. S., Bouchez, J. L., Nédélec A., & Sabaté P. (2004). Evidence of an early NS magmatic event in the Paleoproterozoic Teofilandia granitoids (Sao Francisco Craton, Brazil): a combined microstructural and magnetic fabric study. *Precambrian Research, 134*(1-2), 41–59.

Dong, S., Zhang, Y., Zhang, F., Cui, J., Chen, X., Zhang, S., et al. (2015). Late Jurassic–Early Cretaceous continental convergence and intracontinental orogenesis in East Asia: a synthesis of the Yanshan revolution. *Journal of Asian Earth Sciences, 114,* 750–770. https://doi.org/10.1016/j.jseaes.2015.08.011

Dou, J.-Z., Zhang, H.-F., Tong, Y., Wang, F., Chen, F.-K., & Li, S.-R. (2018). Application of geothermo-barometers to Mesozoic granitoids in the Jiaodong Peninsula, eastern China: Criteria for selecting methods of pressure estimation and implications for crustal exhumation. *Journal of Asian Earth Sciences, 160*, 271–286. https://doi.org/10.1016/j.jseaes.2018.01.019

Dunlop, D. J. (2002). Theory and application of the Day plot (Mrs/Ms versus Hcr/Hc) 1. Theoretical curves and tests using titanomagnetite data. *Journal of Geophysical Research, 107*(B3). https://doi.org/10.1029/2001jb000486

Faure, M., Lin, W., & Breton, N. L. (2001). Where is the North China-South China boundary in eastern China? *Geology, 29*(2), 119–122. https://doi.org/10.1130/0091-7613(2001)029<0119:WITNCS>2.0.CO;2

Faure, M., Lin, W., & Chen, Y. (2012). Is the Jurassic (Yanshanian) intraplate tectonics of north China due to westward indentation of the North China Block? *Terra Nova*, *24*(6), 456–466. https://doi.org/10.1111/ter.12002

Faure, M., Lin, W., Monié, P., Le Breton, N., Poussineau, S., Panis, D., et al. (2003). Exhumation tectonics of the ultrahigh-pressure metamorphic rocks in the Qinling orogen in east China: New petrological-structural-radiometric insights from the Shandong Peninsula. *Tectonics, 22*(3), 1018. https://doi.org/10.1029/2002TC001450

Gébelin, A., Martelet, G., Chen, Y., Brunel, M., & Faure, M. (2006). Structure of late Variscan Millevaches leucogranite massif in the French Massif Central: AMS and gravity modeling results. *Journal of Structural Geology, 28*(1), 148–169. https://doi.org/10.1016/j.jsg.2005.05.021

Goss, S. C., Wilde, S. A., Wu, F., & Yang, J. (2010). The age, isotopic signature and significance of the youngest Mesozoic granitoids in the Jiaodong terrane, Shandong province, North China Craton. *Lithos, 120*(3), 309–326. https://doi.org/10.1016/j.lithos.2010.08.019

Gueydan, F., Morency, C., & Brun, J. P., 2008. Continental rifting as a function of lithosphere mantle strength. *Tectonophysics, 460,* 83–93. https://doi.org/10.1016/j.tecto.2008.08.012

Guineberteau, B., Bouchez, J. L., & Vigneresse, J. L. (1987). The Mortagne granite pluton (France) emplaced by pull-apart along a shear zone: Structural and gravimetric arguments and regional implication. *Geological Society of America Bulletin, 99*(6), 763–770. https://doi.org/10.1130/0016-7606

Guo, J. H., Chen, F. K., Zhang, X. M., Siebel, W., & Zhai, M. G. (2005). Evolution of syn- to post-collisional magmatism from north Sulu UHP belt, eastern China: zircon U-Pb geochronology. *Acta Petrologica Sinica, 21*(4), 1281–1301. (in Chinese with English abstract)

Guo, Z. X., Zhao, X. Z., Yang, Y. T., Zhang, R. F., Han, C. Y., Shi, Y. P., et al. (2018). Jurassic–earliest Cretaceous tectonostratigraphic evolution of the Erlian Basin, Northeast China: Records of polyphase intracontinental deformation in Northeast Asia. *Marine and Petroleum Geology, 96*, 405–428. https://doi.org/10.1016/j.marpetgeo.2018.06.013

Hacker, B. R., Wallis, S. R., Mcwilliams, M. O., & Gans, P. B. (2009). ^{40}Ar/^{39}Ar constraints on the tectonic history and architecture of the ultrahigh-pressure Sulu orogen. *Journal of Metamorphic Geology, 27*(9)*,* 827–844. https://doi.org/10.1111/j.1525-1314.2009.00840.x

Hacker, B. R., Wallis, S. R., Ratschbacher, L., Grove, M. & Gehrels, G., (2006). High-temperature geochronology constraints on the tectonic history and architecture of the ultrahigh-pressure Dabie-Sulu Orogen. *Tectonics, 25*, TC5006. https://doi.org/10.1029/2001JB001129/2005TC001937

He, Z.J., Li, J.Y., Niu, B.G., & Ren, J.S. (1998). A Late Jurassic intense thrusting-uplifting event in the Yanshan–Yinshan area, northern China, and its sedimentary response. *Geological Review 44*, 407–418.

Hu, F., Fan, H., Yang, J., Wan, Y., Liu, D., Zhai, M., et al. (2004). Mineralizing age of the Rushan lode gold deposit in the Jiaodong Peninsula: SHRIMP U-Pb dating on hydrothermal zircon. *Chinese Science Bulletin, 49*(15), 1629–1636. https://doi.org/10.1007/bf03184134

Hrouda, F., & Kahan, štefan. (1991). The magnetic fabric relationship between sedimentary and basement nappes in the High Tatra Mountains, N. Slovakia. *Journal of Structural Geology, 13*(4), 431–442. https://doi.org/10.1016/0191-8141(91)90016-c

Jahn, B. M., Liu, D., Wan, Y., Song, B., & Wu, J. (2008). Archean crustal evolution of the Jiaodong Peninsula, China, as revealed by zircon SHRIMP geochronology, elemental and Nd-isotope geochemistry. *American Journal of Science, 308*(3), 232–269. https://doi.org/10.2475/03.2008.03

Jelinek, V. (1978). Statistical processing of anisotropy of magnetic susceptibility measured on groups of specimens. *Studia Geophysica et Geodaetica, 22*(1), 50–62. https://doi.org/10.1007/BF01613632

Jelinek, V. (1981). Characterization of the magnetic fabric of rocks. *Tectonophysics, 79*, 63–67. https://doi.org/10.1016/0040-1951(81)90110-4

Ji, W., Chen, Y., Chen, K., Wei, W., Faure, M., & Lin, W. (2018b). Multiple emplacement and exhumation history of the late mesozoic dayunshan–mufushan batholith in southeast china and its tectonic significance: 2. magnetic fabrics and gravity survey. *Journal of Geophysical Research: Solid Earth, 123*, 711–731. https://doi.org/10.1002/ 2017JB014597

Ji, W., Faure, M., Lin, W., Chen, Y., Chu, Y., & Xue, Z. (2018a). Multiple emplacement and exhumation history of the Late Mesozoic Dayunshan–Mufushan batholith in southeast China and its tectonic significance: 1. Structural analysis and geochronological constraints. *Journal of Geophysical Research: Solid Earth, 123*, 689–710. https://doi.org/10.1002/2017JB014597

Kratinová, Z., Závada, P., Hrouda, F., & Schulmann, K. (2006). Non-scaled analogue modelling of AMS development during viscous flow: A simulation on diapir-like structures. *Tectonophysics,* *418*(1), 51–61. https://doi.org/10.1016/j.tecto.2005.12.013

Laske, G., Masters, G., Ma, Z., & Pasyanos, M. (2013). Update on CRUST1.0 — A1-Degree Global Model of Earth's Crust. EGU General Assembly Conference Abstracts.

Leier, A. L., Decelles, P. G., Kapp, P., & Gehrels, G. E. (2007). Lower Cretaceous strata in the Lhasa Terrane, Tibet, with implications for understanding the early tectonic history of the Tibetan Plateau. *Journal of Sedimentary Research, 77*(9–10), 809–825. http://doi.org/10.2110/jsr.2007.078

Li, J., & Hou, G. (2018). Cretaceous stress field evolution and origin of the Jiaolai Basin, Eastern North China. *Journal of Asian Earth Sciences, 160,* 258–270. https://doi.org/10.1016/j.jseaes.2018.01.024

Li, J. W., Paulo, V., Zhou, M. F., Zhao, X. F., & Ma, C. Q. (2006). Geochronology of the Pengjiakuang and Rushan gold deposits, Eastern Jiaodong Gold province, Northeastern China: Implications for regional mineralization and geodynamic setting. *Economic Geology, 101*(5), 1023–1038. https://doi.org/10.2113/gsecongeo.101.5.1023

Li, X. H. (2000). Cretaceous magmatism and lithospheric extension in southeast China. *Journal of Asian Earth Sciences, 18*, 293–305. https://doi.org/10.1016/S1367-9120(99)00060-7

Li, X. H., Chen, F., Guo, J. H., Li, Q. L., Xie, L. W., & Siebel, W. (2007). South China provenance of the lower-grade Penglai Group north of the Sulu UHP orogenic belt, eastern China: Evidence from detrital zircon ages and Nd-Hf isotopic composition. *Geochemical Journal, 41*, 29–45. https://doi.org/10.2343/geochemj.41.29

Li, J. H., Cawood, P. A., Ratschbacher, L., Zhang, Y., Dong, S., & Xin, Y., et al. (2020). Building Southeast China in the late Mesozoic: Insights from alternating episodes of shortening and extension along the Lianhuashan fault zone. *Earth Sciences Reviews, 201*, 103056.

https://doi.org/10.1016/j.earscirev.2019.103056

Lin, W., Charles, N., Chen, K., Chen, Y., Faure, M., Wu, L., et al. (2013b). Late Mesozoic compressional to extensional tectonics in the Yiwulüshan massif, NE China and its bearing on the evolution of the Yinshan–Yanshan orogenic belt. Part II: Anisotropy of magnetic susceptibility and gravity modeling. *Gondwana Research*, *23*(1), 78–94. https://doi.org/10.1016/j.gr.2012.02.012

Lin, W., Faure, M., Chen, Y., Ji, W. B., Wang, F., Wu, L., et al. (2013a). Late Mesozoic compressional to extensional tectonics in the Yiwulüshan massif, NE China and its bearing on the evolution of the Yinshan–Yanshan orogenic belt. Part I: Structural analyses and geochronological constraints. *Gondwana Research*, *23*(1), 54–77. https://doi.org/10.1016/j.gr.2012.02.013

Lin, W., Monié, P., Faure, M., Schärer, U., Shi, Y. H., Le Breton, N., & Wang, Q. C. (2011). Cooling paths of the NE China crust during the Mesozoic extensional tectonics: Example from the south-Liaodong peninsula metamorphic core complex. *Journal of Asian Earth Sciences*, *42*(5), 1048–1065. https://doi.org/10.1016/j.jseaes.2010.09.007

Lin, W., & Wei, W. (2018). Late Mesozoic extensional tectonics in the North China Craton and its adjacent regions: a review and synthesis. *International Geology Review*, 1–29. https://doi.org/10.1080/00206814.2018.1477073

Liu, F. L., & Liou, J. G. (2011). Zircon as the best mineral for P–T–time history of UHP metamorphism: A review on mineral inclusions and U–Pb SHRIMP ages of zircons from the Dabie–Sulu UHP rocks. *Journal of Asian Earth Sciences, 40*(1), 1–39. https://doi.org/10.1016/j.jseaes.2010.08.007

Liu, F., Liu, L., Liu, P., Wang, F., Cai, J., Liu, J., et al. (2017a). A relic slice of Archean–early Paleoproterozoic basement of Jiaobei Terrane identified within the Sulu UHP belt: Evidence from protolith and metamorphic ages from meta-mafic rocks, TTG–granitic gneisses, and metasedimentary rocks in the Haiyangsuo region. *Precambrian Research, 303,* 117–152. https://doi.org/10.1016/j.precamres.2017.03.014

Liu, H., Martelet, G., Wang, B., Erdmann, S., Chen, Y., & Faure, M., et al. (2018). Incremental emplacement of the Late Jurassic midcrustal, lopolith-like Qitianling pluton, South China, revealed by AMS and Bouguer gravity data. *Journal of Geophysical Research: Solid Earth, 123*. https://doi.org/10.1029/2018JB015761

Liu, J. L., Shen, L., Ji, M., Guan, H. M., Zhang, Z. C., & Zhao, Z. D. (2013). The Liaonan/Wanfu metamorphic core complexes in the Liaodong Peninsula: Two stages of exhumation and constraints on the destruction of the North China Craton. *Tectonics*, *32*(5), 1121–1141. https://doi.org/10.1002/tect.20064

Liu, L. P., Li, Z.-X., Danišík, M., Li, S., Evans, N., Jourdan, F., & Tao, N. (2017b). Thermochronology of the Sulu ultrahigh-pressure metamorphic terrane: Implications for continental collision and lithospheric thinning. *Tectonophysics, 712-713*, 10–29. https://doi.org/10.1016/j.tecto.2017.05.003

Ma, A., Hu, X., Garzanti, E., Han, Z., & Lai, W. (2017). Sedimentary and tectonic evolution of the Southern Qiangtang basin: implications for the Lhasa-Qiangtang collision timing. *Journal of Geophysical Research Solid Earth*, 122. https://doi.org/10.1002/2017JB014211.

Maruyama, S., Isozaki, Y., Kimura, G., & Terabayashi, M. (1997). Paleogeographic maps of the Japanese Islands: Plate tectonic synthesis from 750 Ma to present: *Island Arc, 6*, 121–142. https://doi.org/10.1111/j.1440-1738.1997. tb00043.x

Meng, Q. R. (2003). What drove late Mesozoic extension of the northern China–Mongolia tract? *Tectonophysics, 369*(3–4), 155–174. https://doi.org/10.1016/S0040-1951(03)00195-1

Menzies, M. A, Fan, W, & Zhang, M. (1993). Palaeozoic and Cenozoic lithoprobes and the loss of >120 km of Archaean lithosphere, Sino-Korean craton, China. M*agmatic Processes and Plate Tectonics, 76*(1), 71–81. http://dx.doi.org/10.1144/GSL.SP.1993.076.01.04

Miller, R. B., & Paterson, S. R. (1994). The transition from magmatic to high-temperature solid-state deformation: implications from the Mount Stuart batholith, Washington. *Journal of Structural Geology, 16*(6), 853–865. https://doi.org/10.1016/0191-8141(94)90150-3

Miller, R. B., Paterson, S. R., & Matzel, J. P. (2009). Plutonism at different crustal levels: Insights from the ~5–40 km (paleodepth) North Cascades crustal section, Washington. *Geological Society of America Special Paper, 456,* 125–149. https://doi.org/10.1130/2009.2456(05)

Paterson, S. R., Ardilla, K., Vernon, R., & Žák, J. (2019). A review of mesoscopic magmatic structures and their potential for evaluating the hypersolidus evolution of intrusive complexes. *Journal of Structure Geology, 125*, 134–147. https://doi.org/10.1016/j.jsg.2018.04.022

Paterson, S. R., Fowler, T. K., Schmidt, K. L., Yoshinobu, A. S., Yuan, E. S., & Miller, R. B. (1998). Interpreting magmatic fabric patterns in plutons. *Lithos, 44*(1–2), 53–82. https://doi.org/10.1016/S0024-4937(98)00022-X

Passchier, C. W., & Trouw, R. A. J. (Eds.). (2005). Microtectonics. Berlin: Springer

Qiu, L., Kong, R., Yan, D. P., Wells, M. L., Wang, A., Sun, W., et al. (2018). The Zhayao tectonic window of the Jurassic Yuantai thrust system in Liaodong Peninsula, NE China: Geometry, kinematics and tectonic implications. *Journal of Asian Earth Sciences, 164*, 58–71. https://doi.org/10.1016/j.jseaes.2018.06.012

Rabillard, A., L. Arbaret, L. Jolivet, N. Le Breton, C. Gumiaux, R. Augier, et al. (2015). Interactions between plutonism and detachments during metamorphic core complex formation, Serifos Island (Cyclades, Greece), *Tectonics, 34*, 1080–1106, https://doi.org/10.1002/2014TC003650

Ratschbacher, L., Hacker, B. R., Webb, L. E., McWilliams, M., Ireland, T., Dong, S., et al. (2000). Exhumation of the ultrahigh-pressure continental crust in east central China: Cretaceous and Cenozoic unroofing and the Tan-Lu fault. *Journal of Geophysical Research: Solid Earth, 105*(B6), 13303–13338. https://doi.org/10.1029/2000jb900040

Ren, J., Tamaki, K., Li, S., & Junxia, Z. (2002). Late Mesozoic and Cenozoic rifting and its dynamic setting in Eastern China and adjacent areas. *Tectonophysics, 344*, 175–205. https://doi.org/10.1016/s0040-1951(01)00271-2

Roure, F., Choukroune, P., Berastegui, X., Munoz, J.A., Villien, A., & Matheron, P., et al. (1989). ECORS Deep seismic data and balanced cross sections: geometric constraints on the evolution of the Pyrenees. *Tectonics, 8*, 41–50. https://doi.org/10.1029/TC008i001p00041

Schmid, S. M., & Casey, M. (1986). Complete fabric analysis of some commonly observed quartz c-axis patterns. In Hobbs, B.E., Heard, H.C. (Eds.), Mineral and Rock Deformation: Laboratory Studies (pp. 246–261). American Geophysical Union.

Shen, Y. C., Xie, H. Y., Li, G. M., Liu, T. B., Sun, X. Y., & Wang, Y. J. (1998). Geology and prospecting of the Pengjiakuang gold deposit, Shandong. *Geology and Prospecting, 34*(5), 3–13. (in Chinese with English abstract)

Stipp, M., Stuenitz, H., Heilbronner, R., & Schmid, S. M. (2002). The eastern Tonale fault zone: a nature laboratory for crystal plastic deformation of quartz over a temperature range from 250 to 700°C. *Journal of Structural Geology 5*, 1–24. https://doi.org/10.1016/S0191-8141(02)00035-4

Tam, P. Y., Zhao, G., Liu, F., Zhou, X., Sun, M., & Li, S. (2011). Timing of metamorphism in the Paleoproterozoic Jiao-Liao-Ji belt: new SHRIMP U–Pb zircon dating of granulites, gneisses and marbles of the Jiaobei massif in the North China Craton. *Gondwana Research, 19*(1), 150–162. https://doi.org/10.1016/j.gr.2010.05.007

Tang, H., Zheng, J., Yu, C., Ping, X., & Ren, H. (2014). Multistage crust–mantle interactions during the destruction of the North China Craton: Age and composition of the Early Cretaceous intrusions in the Jiaodong Peninsula. *Lithos, 190–191*, 52–70. https://doi.org/10.1016/j.lithos.2013.12.002

Trindade, R. I. F., Raposo, M. I. B., Ernesto, M., & Siqueira, R. (1999). Magnetic susceptibility and partial anhysteretic remanence anisotropies in the magnetite-bearing granite pluton of Tourão, NE Brazil. *Tectonophysics, 314*(4), 443–468. https://doi.org/10.1016/S0040-1951(99)00220-6

Turrillot, P., Faure, M., Martelet, G., Chen, Y., & Augier, R. (2011). Pluton-dyke relationships in a Variscan granitic complex from AMS and gravity modeling. Inception of the extensional tectonics in the South Armorican Domain (France). *Journal of Structural Geology, 33,* 1681–1698. https://doi.org/10.1016/j.jsg.2011.08.004

Van der Voo, R., Van Hinsbergen, D. J. J., Domeier, M., Spakman, W., & Torsvik, T. H. (2015). Latest Jurassic–earliest Cretaceous closure of the Mongol–Okhotsk Ocean: A paleomagnetic and seismological–tomographic analysis. *Geological Society of America Special Papers, 513*, 589–606. https://doi.org/10.1130/2015.2513(19)

Vernon, R. H. (2000). Review of microstructural evidence of magmatic and solid-state flow. *Electronic Geosciences, 5*, 1–23. https://doi.org/10.1007/s10069-000-0002-3

Vigneresse, J. L. (1990). Use and misuse of geophysical data to determine the shape at depth of granitic intrusions. *Geological Journal, 25*(3–4), 249–260. https://doi.org/10.1002/gj.3350250308

Vigneresse, J. L. (1995). Crustal regime of deformation and ascent of granitic magma. *Tectonophysics, 249*(3-4), 187–202. https://doi.org/10.1016/0040-1951(95)00005-8

Vigneresse, J. L., & Bouchez, J. L. (1997). Successive granitic magma batches during pluton emplacement: the case of Cabeza de Araya (Spain). *Journal of Petrology, 38*(12), 1767–1776. https://doi.org/10.1093/petroj/38.12.1767

Wallis, S. R., Ishiwatari, A., Hirajima, T., Ye, K., Guo, J., Nakamura, D., et al. (1997). Occurrence and field relationships of ultrahigh-pressure metagranitoid and coesite eclogite in the Su-Lu terrane, eastern China. *Journal of the Geological Society, 154*(1), 45–54. https://doi.org/10.1144/gsjgs.154.1.0045

Wan, Y., Song, B., Liu, D., Wilde, S. A., Wu, J., & Zhou, H. (2006). SHRIMP U–Pb zircon geochronology of Palaeoproterozoic metasedimentary rocks in the North China Craton: evidence for a major Late Palaeoproterozoic tectonothermal event. *Precambrian Research,149*(3–4)*,* 249–271. https://doi.org/10.1016/j.precamres.2006.06.006

Wang, J., Chang, S.-C., Lu, H.-B., & Zhang, H.-C. (2015). Detrital zircon provenance of the Wangshi and Laiyang groups of the Jiaolai basin: evidence for Early Cretaceous uplift of the Sulu orogen, Eastern China. *International Geology Review, 58*(6)*,* 719–736. https://doi.org/10.1080/00206814.2015.1105728

Wang, Q., Ishiwatari, A., Zhao, Z., Hirajima, T., Hiramatsu, N., Enami, M., et al. (1993). Coesite-bearing granulite retrograded from eclogite in Weihai, Eastern China, *European Journal of Mineralogy, 5*(1), 141–152. https://doi.org/10.1127/ejm/5/1/0141

Wang, T., Guo, L., Zheng, Y., Donskaya, T., Gladkochub, D., Zeng, L., et al. (2012). Timing and processes of late Mesozoic mid-lower-crustal extension in continental NE Asia and implications for the tectonic setting of the destruction of the North China Craton: mainly constrained by zircon U–Pb ages from metamorphic core complexes. *Lithos*, *154*(6), 315–345. https://doi.org/10.1016/j.lithos.2012.07.020

Wei, W., Chen, Y., Faure, M., Shi, Y., Martelet, G., Hou, Q., et al. (2014a). A multidisciplinary study on the emplacement mechanism of the Qingyang-Jiuhua massif in Southeast China and its tectonic bearings. Part I: Structural geology, AMS and paleomagnetism. *Journal of Asian Earth Sciences,* *86*, 76–93. https://doi.org/10.1016/j.jseaes.2013.06.003

Wei, W., Chen, Y., Faure, M., Martelet, G., Lin, W., Wang, Q., et al. (2016). An early extensional event of the South China Block during the Late Mesozoic recorded by the emplacement of the Late Jurassic syntectonic Hengshan Composite Granitic Massif (Hunan, SE China). *Tectonophysics, 672–673*, 50–67. http://dx.doi.org/10.1016/j.tecto.2016.01.028

Wei, W., Martelet, G., Le Breton, N., Shi, Y., Faure, M., Chen, Y., et al. (2014b). A multidisciplinary study of the emplacement mechanism of the Qingyang-Jiuhua massif in Southeast China and its tectonic bearings. Part II: Amphibole geobarometry and gravity modeling. *Journal of Asian Earth Sciences, 86*, 94–105. https://doi.org/10.1016/j.jseaes.2013.09.021

Wernicke, B., & Axen, G. J. (1988). On the role of isostasy in the evolution of normal fault systems. *Geology, 16*, 848–851. http://dx.doi.org/10.1130/0091-7613(1988)016<0848:OTROII>2.3.CO;2.

Wong, W. H. (2009). The Mesozoic Orogenic Movement in Eastern China. *Bulletin of the Geological Society of China, 8*(1), 33–44. http://dx.doi.org/10.1111/j.1755-6724.1929.mp8001004.x

Wu, F. Y., Yang, J. H., Xu, Y. G., Wilde, S. A., & Walker, R. J. (2019). Destruction of the North China Craton in the Mesozoic. *Annual Review of Earth and Planetary Sciences, 47(1)*, 73–95. https://doi.org/10.1146/annurev-earth-053018-060342

Wu, L. (2014). The Mesozoic-Cenozoic thermal evolution of the Sulu Orogenic Belt: Constraints from low-temperature thermochronology, (Doctoral dissertation). Retrieved from Dissertation Knowledge discovery system (http://dpaper.las.ac.cn/Dpaper/homeNew). Institute of Geology and Geophysics, Chinese Academy of Sciences.

Wu, L., Monié, P., Wang, F., Lin, W., Ji, W., & Yang, L. (2018). Multi-phase cooling of Early Cretaceous granites on the Jiaodong Peninsula, East China: Evidence from ^{40}Ar/^{39}Ar and

(U-Th)/He thermochronology. *Journal of Asian Earth Sciences, 160,* 334–347. https://doi.org/10.1016/j.jseaes.2017.11.014

Xia, Z. M., Liu, J. L., Ni, J. L., Zhang, T. T., Shi, X. M., & Yun, W. (2016). Structure, evolution and regional tectonic implications of the Queshan metamorphic core complex in eastern Jiaodong Peninsula of China. *Science China Earth Sciences, 59*(5), 997–1013. https://doi.org/ 10.1007/s11430-015-5259-3

Xu, Y. G. (2001). Thermo-tectonic destruction of the Archaean lithospheric keel beneath the Sino-Korean Craton in China: evidence, timing and mechanism. *Physics and Chemistry of the Earth, Part A: Solid Earth and Geodesy, 26*(9–10), 747–757. https://doi.org/10.1016/S1464-1895(01)00124-7

Xue, Z., Martelet, G., Lin, W., Faure, M., Chen, Y., Wei, W., et al. (2017). Mesozoic crustal thickening of the Longmenshan belt (NE Tibet, China) by imbrication of basement slices: Insights from structural analysis, petrofabric and magnetic fabric studies, and gravity modeling. *Tectonics, 36*, 3110–3134. https://doi.org/10.1002/2017TC004754

Yang, J., Wu, F., Wilde, S., Belousova, E., & Griffin, W. (2008). Mesozoic decratonization of the North China Block. *Geology, 36*(6), 467–470. https://doi.org/10.1130/G24518A.1

Yin, A. (2004). Gneiss domes and gneiss dome systems. *Geological Society of America Special Paper 380*: Gneiss Domes in Orogeny, 1–14. https://doi.org/10.1130/0-8137-2380-9.1

Yoshinobu, A. S., Okaya, D. A., & Paterson, S. R. (1998). Modelling the thermal evolution of fault-controlled magma emplacement models: *Journal of Structural Geology, 20*, 1205–1218. https://doi.org/10.1016/S0191-8141(98)00064-9

Žák, J., Verner, K., Sláma, J., Kachlík, V., & Chlupáčová, M. (2013). Multistage magma emplacement and progressive strain accumulation in the shallow-level Krkonoše-Jizera plutonic complex, Bohemian massif. *Tectonics, 32*(5), 1493–1512. https://doi.org/10.1002/tect.20088

Žák, J., Verner, K., Tomek, F., Holub, F. V., Johnson, K., & Schwartz, J. J. (2015). Simultaneous batholith emplacement, terrane/continent collision, and oroclinal bending in the Blue Mountains province, North American Cordillera. *Tectonics, 34*(6), 1107–1128. https://doi.org/10.1002/2015TC003859

Zhai, M., Cong, B., Guo, J., Liu, W., Li, Y., & Wang, Q. (2000). Sm–Nd geochronology and petrography of garnet pyroxene granulites in the Northern Sulu region of China and their geotectonic implication. *Lithos, 52*, 23–33. https://doi.org/10.1016/s0024-4937(99)00082-1

Zhang, D. Q., Xu, H. L., & Sun, G, Y. (1995). Emplacement ages of the Denggezuang gold deposit and the Kunyushan granite and their geological implications. *Geological Review, 41*(5)*,* 415–425. https://doi.org/10.16509/j.georeview.1995.05.004 (in Chinese with English abstract)

Zhang, J., Zhao, Z. F., Zheng, Y. F., & Dai, M. (2010). Postcollisional magmatism: Geochemical constraints on the petrogenesis of Mesozoic granitoids in the Sulu orogen, China. *Lithos, 119*(3–4)*,* 512–536. https://doi.org/10.1016/j.lithos.2010.08.005

Zhang, H. Y., Hou, Q. L., & Cao, D. Y. (2007). Study of thrust and nappe tectonics in the eastern Jiaodong Peninsula, China. *Science China Earth Sciences, 50*(2)*,* 161–171.

Zhang, K., Lü, Q., Yan, J., Hu, H., Fu, G.M., &Shao, L. (2018). Crustal structure beneath the Jiaodong Peninsula, North China, revealed with a 3D inversion model of magnetotelluric data. *Journal of Geophysics and Engineering, 15*, 2442–2454. https://doi.org/10.1088/1742-2140/aaca5e

Zhang, S., Zhu, G., Xiao, S., Su, N., Liu, C., Wu X., et al. (2020). Temporal variations in the dynamic evolution of an overriding plate: Evidence from the Wulong area in the eastern North China Craton, China. The Geological Society of America, in press. https://doi.org/10.1130/B35465

Zhang, S. B., Tang, J., & Zheng, Y. F. (2014). Contrasting Lu–Hf isotopes in zircon from Precambrian metamorphic rocks in the Jiaodong Peninsula: constraints on the tectonic suture between North China and South China. *Precambrian Research, 245*(5), 29–50. https://doi.org/10.1016/j.precamres.2014.01.006

Zhang, T., & Zhang, Y. (2007). Geochronological sequence of Mesozoic intrusive magmatism in Jiaodong Peninsula and its tectonic constraints. *Geological Journal of China Universities, 13*(2), 323–336. https://doi.org/10.16108/j.issn1006-7493.2007.02.015 (in Chinese with English abstract)

Zhang, T., & Zhang, Y. (2008). Late Mesozoic tectono-magmatic evolution history of the Jiaobei uplift, Shandong Peninsula. *Acta Geologica Sinica, 82*(9), 1220–1228. (in Chinese with English abstract)

Zhao, R., Wang, Q., Liu, X., Wang, W., & Pan, R. (2016). Architecture of the Sulu crustal suture between the North China Craton and Yangtze Craton: constraints from Mesozoic granitoids. *Lithos, 266–267*, 348–361. https://doi.org/10.1016/S0169-1368(97)00022-X

Zhu, G., Chen, Y., Jiang, D., & Lin, S. (2015). Rapid change from compression to extension in the North China Craton during the early Cretaceous: evidence from the Yunmengshan metamorphic core complex. *Tectonophysics, 656*(1), 91–110. https://doi.org/10.1016/j.tecto.2015.06.009

Zhu, R. X., Chen, L., Wu, F. Y., Liu, J. L. (2011). Timing, scale and mechanism of the destruction of the North China Craton. *Science China Earth Sciences, 54*, 789–797.

Figure captions

Figure 1. Tectonic sketch of the northern part of Jiaodong Peninsula (after Faure et al., 2003a) with the location of the study area. Abbreviations: Y: Yuangezhuang pluton; Q: Que pluton; H: Haiyang pluton; K: Kunyu pluton; S: Sanfo pluton; W: Weide pluton.

Figure 2. Simplified geological map of the Que-Kunyu-Yuangezhuang-Sanfo (QKYS) massif. Structural foliations and lineations based on our field work show the domal architecture of the massif. Abbreviations are same as the Figure 1.

Figure 3. Geological cross-sections across the QKYS massif (locations are shown in Figure 2). A: Cross-section drawn parallel to the direction of the SW–NE. B and C: WNW–ESE cross-sections parallel to the direction of the ductile deformation in the western margin.

Figure 4. Available geochronological data of the QKYS massif. All the data are collected from previous studies (Figure legends and abbreviations are the same in Figure 2). A: Zircon U-Pb ages of the Late Mesozoic plutons. B: Density plot of zircon U-Pb ages from the Late Mesozoic plutons showing their peak ages. C: $^{40}Ar/^{39}Ar$ cooling ages of the massif.

Figure 5. Field photographs of the Late Jurassic and Early Cretaceous plutons. A: Late Jurassic Kunyu foliated biotite monzogranite (18JD59: 37.3275°N, 121.7749°E). B: Late Jurassic Que mylonitic granite (QS43: 37.1231°N, 121.3873°E). C: Late Jurassic Kunyu undeformed biotite monzogranite (KY20: 37.1109°N, 121.7139°E). D: Early Cretaceous undeformed porphyritic biotite monzogranite with large K-feldspar phenocrysts (YG10: 37.2880°N, 121.4306°E).

Figure 6. Field structures represented as equal-area lower hemisphere diagrams of the planar and linear structures related to the ductile deformation developed in the QKYS massif.

Figure 7. Field and microscope photos of the deformed granite in the north margin of the K pluton and gneissic country rocks, displaying a top-to-the-NE sense of shear. A: NE–SW trending mineral lineation marked in the gneissic country rocks by aggregates of the biotite and quartz (19JD127: 37.3786°N, 121. 7445°E). B: Sigma-type felsic grains in the orthogneiss (19JD127: 37.3786°N, 121. 7445°E). C: Sigma-type feldspars in the granite (KY57: 37.2789°N, 121.8502°E). D: In the gneiss (17JD35:37.3415°N, 121.7575°E), quartz and feldspars showing sigma-type features. Symbols: Qz: quartz; Pl: plagioclase; Bi: biotite; Amp: amphibole.

Figure 8. Field, hand-sample and microscope photos of the metamorphic rocks from the south of the QKYS massif, all showing a top-to-SW shearing. A: ENE–WSW mineral lineation marked by mineral aggregates in a mylonite (18JD28: 36.8016°N, 121.5354°E). B: Isoclinal fold axes parallel to a N50° stretching lineation formed by muscovite and feldspar aggregates (18JD29: 36.7503°N, 121.5576°E). C: Asymmetric felsic boudins within the micaschist (18JD29: 36.7503°N, 121.5576°E). D: Sigma-type feldspar porphyroclasts in a felsic mylonite (18JD28: 36.8016°N, 121.5354°E). E: Sigma-type feldspar porphyroclasts in the mylonite (18JD28: 36.8016°N, 121.5354°E). F: Microphotograph of the sigma-type feldspar porphyroclasts in a felsic mylonite (18JD13: 36.8309°N, 283 121.4490°E). G: Microphotograph of muscovite "fish" in a micaschist (18JD29: 36.7503°N, 121.5576°E) showing the same asymmetry. Symbols: Qz: quartz; Pl: plagioclase; Mus: muscovite.

Figure 9. Field, hand-sample and microscope photos of the mylonitic Q granite and its host rocks, showing a top-to-the-WNW shearing. A: WNW–ESE trending lineation defined by biotite and feldspar aggregates in the granite (QS29: 37.1317°N, 121. 2507°E). B: Asymmetric and top-to-the-WNW sheared felsic lenses in the meta-sedimentary rock (QS37: 37.0279°N, 121.3374°E). C: Sigma-type feldspar porphyroclasts in the granite (QS28: 37.1598°N, 121. 2585°E). D: S-C fabric and sigma-type feldspar porphyroclasts in the granite (QS43: 37.1231°N, 121.3873°E). E: Thin section: sigma- and delta-type porphyroclasts in the granite (QS41: 37.0995°N, 121.3943°E). F: Thin section: asymmetric feldspar porphyroclast surrounded by fine-grained quartz grain in the granite (QS28: 37.1598°N, 121. 331 2585°E). Symbols: Qz: quartz; Pl: plagioclase; Kfs: K-feldspar; Bi: biotite.

Figure 10. Typical microphotographs showing the microstructures of the QKYS massif. A: Typical magmatic fabric with undeformed quartz, plagioclase, biotite and K-feldspar (SF02: 36.9333°N, 121.6890°E). B: Quartz-veinlet cross-cutting a plagioclase with undulatory extinction, pointing to the deformation ended at relatively low temperature and rather high stress (KY09: 37.2360°N, 121.9220°E). C: Development of myrmekites on feldspar interiors (QS19: 37.1395°N, 121.4491°E). D: K-feldspar

phenocrysts surrounded by "ribbon-like" quartz grains with straight boundaries (KY57: 37.2789°N, 121.8502°E). E: The quartz grains are recrystallized to form the new grains with irregular boundaries, showing the shape preferred orientation (QS40: 37.0989°N, 121.3904°E). F: A very low-grade mylonite, showing the broken K-feldspar as the foliated matrix with no recrystallized quartz (18JD28: 37.2144°N, 121.3871°E). Symbols: Qz: quartz; Pl: plagioclase; Kfs: K-feldspar; Bi: biotite; Myr: myrmekite.

Figure 11. Kinematic map for the tectonic events in the QKYS massif and quartz LPO diagrams obtained by universal stage measurement (Figure captions are the same in Figure 2). Arrows point to the sense of shear of the upper layer over the lower layer. Samples are foliated or mylonitic monzogranite (KY05, KY09, KY57, QS27, QS30, QS43, 18JD125), mylonitic gneiss (18JD13, 18JD18 and 18JD28) and mica-schist (QS37 and 18JD29). All diagrams are lower hemisphere Schmidt net drawn in the XZ section of the bulk strain ellipsoid (*i.e.,* perpendicular to foliation and parallel to the mineral and stretching lineation). Contour intervals given as multiple of random distribution are shown for each sample.

Figure 12. The frequency histograms of K_m for all the AMS sites.

Figure 13. Magnetic mineralogy investigations concerning granite plutons in the QKYS massif. A–C: Thermomagnetic curves. D–F: Acquisition of isothermal remanent magnetization.

Figure 14. M_{rs}/M_s versus H_{cr}/H_c diagram to define the size of magnetite. M_{rs}: remanence of saturation magnetization after removing the applied field, M_s: saturation magnetization under applied field, H_{cr}: coercivity of remanence after removing the applied field, H_c: coercivity under applied field. SD: single domain, PSD: pseudu single domain, and MD: multi-domain.

Figure 15. AMS scalar parameters for the analyzed plutons. A: Distribution of P_j within each pluton (Figure captions are the same in Figure 2, and the offset of Zhuwu Fault is restored). B: the diagram of P_j versus K_m showing the absence of correlation between them. C: T versus K_m diagram showing the absence of correlation between them. D: T versus P_j diagram showing the absence of correlation

between them. *T*: shape factor, P_j: anisotropy degree, and K_m: the mean bulk magnetic susceptibility in 10^{-3} SI.

Figure 16. Lower hemisphere equal-area projections of AMS axes for each pluton, with confidence ellipses at 95%. A: Kunyu pluton (K); B: Que pluton (Q); C: Yuangezhuang pluton (Y) and D: Sanfo pluton (S). Small symbols represent each individual specimen and large ones represent the tensorial mean out of 5–7 specimens.

Figure 17. Magnetic fabric maps of the Late Mesozoic plutons in the QKYS massif, showing the magnetic foliations/lineations and corresponding orientation diagrams (of their poles) in each domain. All orientation diagrams are lower hemisphere, equal-area projections.

Figure 18. Residual Bouguer gravity map of the Jiaodong Peninsula obtained by subtraction of a 150 km wavelength regional trend from the original Bouguer gravity map.

Figure 19. Forward gravity modelling across the QKYS massif revealing its deep geometry. Along NE–SW trending profiles (A–E), and NW–SE trending profiles (F–K). The profiles are located in the Figure 18.

Figure 20. Block diagram showing the bulk geometry, kinematics of the QKYS massif and illustrating the polyphase deformation (D_1, D_2 and D_3) and magmatism (Mag_1 and Mag_2).

Figure 21. A possible tectonic scenario implied from the QKYS massif, pointing to episodic extension and compression tectonics. In these diagrams, we considered the emplacement depth of Late Mesozoic plutons (Dou et al., 2018) as the reference to describe the emplacement-exhumation process of massif from deep to shallower crustal level. A (165–150 Ma): Emplacement of Late Jurassic plutons (Mag_1) with the NE–SW trending extension tectonics, coeval with high-temperature top-to-the-NE shearing (D_1); B (150–135 Ma): NE–SW trending compressional deformation with low-temperature top-to-the-SW sense of shear (D_2); C (130–115 Ma): WNW–ESE trending regional extension tectonics corresponding to the low-temperature top-to-the-WNW shearing (D_3) and leading the QKYS massif

exhumed; D (post-115 Ma): Emplacement of Early Cretaceous plutons (Mag_2) controlled by pre-existing fractures and subsequent erosion.

Figure 22. Geodynamic evolution of East China during Late Mesozoic (modified after Ji *et al*., 2018b and Lin & Wei, 2018). The subduction direction of the Izanagi Plate is based on the Maruyama *et al*., 1997. Late Mesozoic episodic crustal extension and compression are caused by the change of the subduction orientation and angle of the Izanagi plate, accompanied with the Mongol-Okhotsk ocean closure. NCC: North China Craton; SCB: South China Block; CAOB: Central Asian orogenic belt; YS–YS: Yinshan–Yanshan fold and thrust belt; JD: Jiaodong Peninsula; TLF: Tan–Lu fault; THS: Taihangshan; Gbk: Gubeikou fault; Sht: Sihetang ductile shear zone; Yw: Yiwulüshan massif; LY–QL: Lingyuan–Qinglong area; LD: Liaodong Peninsula.

Figure 1.

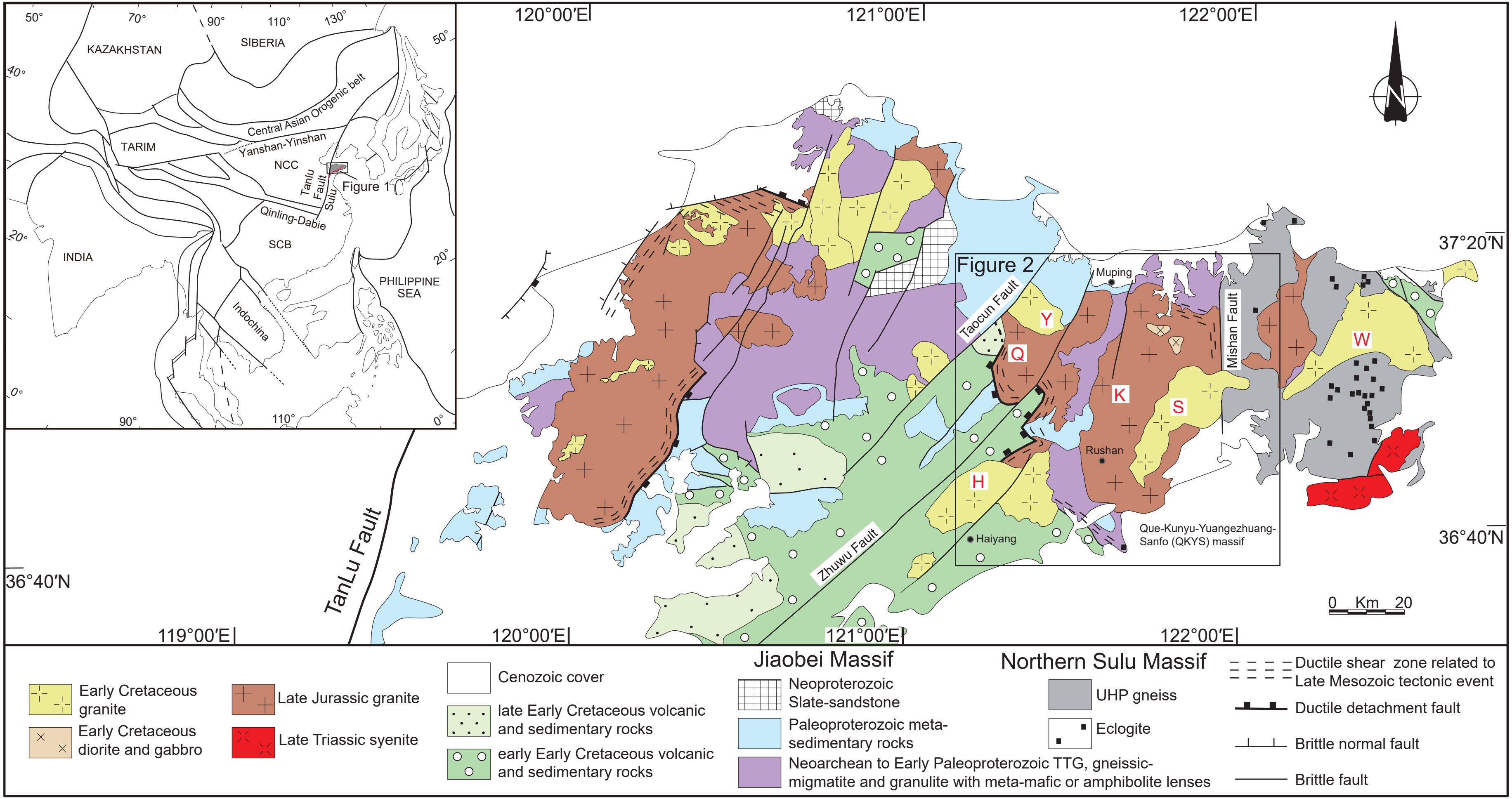
KAZAKHSTAN
SIBERIA
Central Asian Orogenic belt
TARIM
Yanshan-Yinshan
NCC
Tanlu Fault
Sulu
Figure 1
Qinling-Dabie
SCB
INDIA
PHILIPPINE SEA
Indochina
120°00′E
121°00′E
122°00′E
119°00′E
37°20′N
36°40′N
N
Figure 2
Taocun Fault
Muping
Mishan Fault
Y
Q
K
S
W
H
Rushan
Haiyang
Que-Kunyu-Yuangezhuang-Sanfo (QKYS) massif
Zhuwu Fault
TanLu Fault
0 Km 20
Early Cretaceous granite
Early Cretaceous diorite and gabbro
Late Jurassic granite
Late Triassic syenite
Cenozoic cover
late Early Cretaceous volcanic and sedimentary rocks
early Early Cretaceous volcanic and sedimentary rocks
Jiaobei Massif
Neoproterozoic Slate-sandstone
Paleoproterozoic meta-sedimentary rocks
Neoarchean to Early Paleoproterozoic TTG, gneissic-migmatite and granulite with meta-mafic or amphibolite lenses
Northern Sulu Massif
UHP gneiss
Eclogite
Ductile shear zone related to Late Mesozoic tectonic event
Ductile detachment fault
Brittle normal fault
Brittle fault

Figure 2.

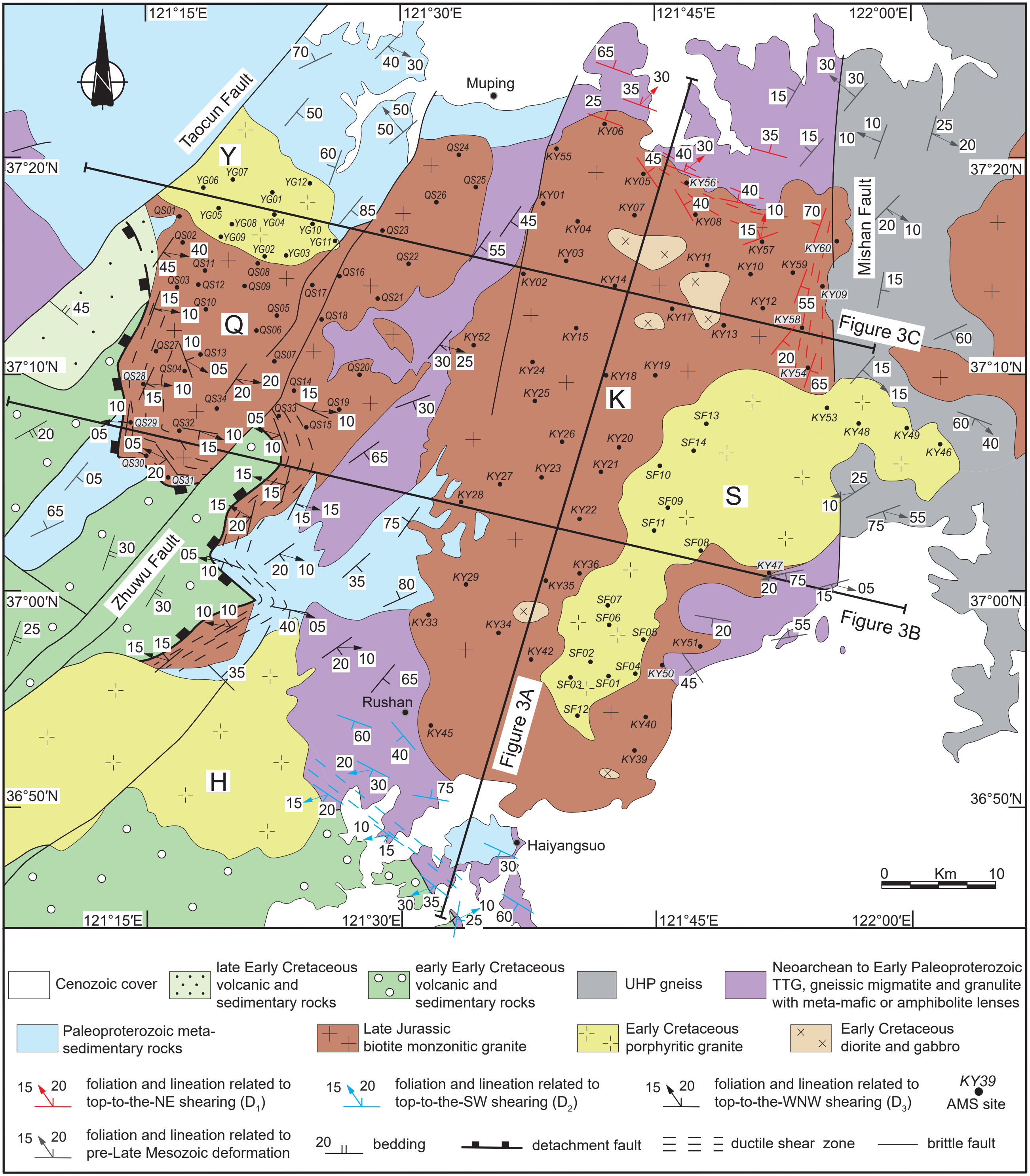

121°15′E
121°30′E
121°45′E
122°00′E
37°20′N
37°10′N
37°00′N
36°50′N
Muping
Rushan
Haiyangsuo
Taocun Fault
Zhuwu Fault
Mishan Fault
Y
Q
K
S
H
Figure 3A
Figure 3B
Figure 3C
0 Km 10
Cenozoic cover
late Early Cretaceous volcanic and sedimentary rocks
early Early Cretaceous volcanic and sedimentary rocks
UHP gneiss
Neoarchean to Early Paleoproterozoic TTG, gneissic migmatite and granulite with meta-mafic or amphibolite lenses
Paleoproterozoic meta-sedimentary rocks
Late Jurassic biotite monzonitic granite
Early Cretaceous porphyritic granite
Early Cretaceous diorite and gabbro
foliation and lineation related to top-to-the-NE shearing (D_1)
foliation and lineation related to top-to-the-SW shearing (D_2)
foliation and lineation related to top-to-the-WNW shearing (D_3)
KY39 AMS site
foliation and lineation related to pre-Late Mesozoic deformation
bedding
detachment fault
ductile shear zone
brittle fault

Figure 3.

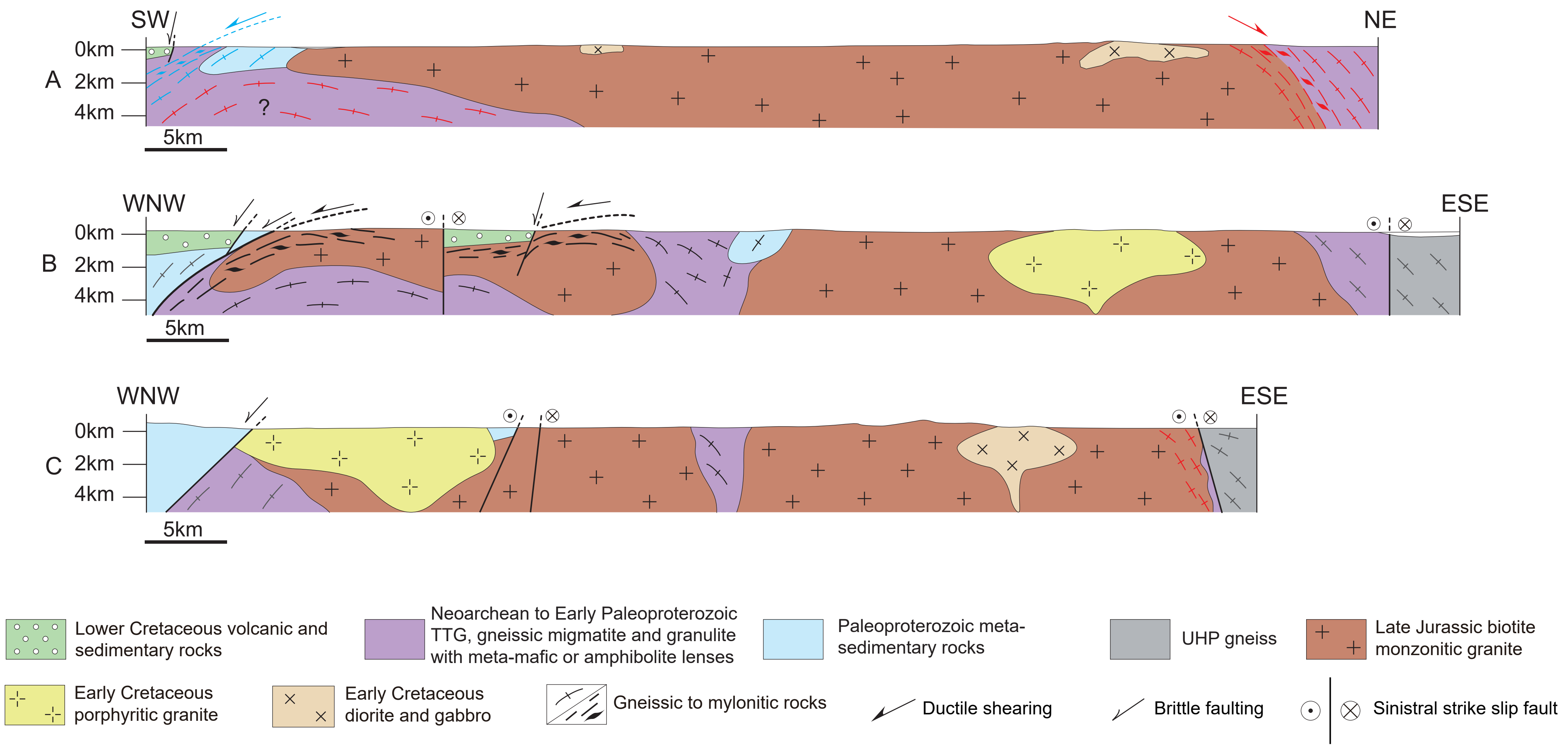

SW
NE
A
0km
2km
4km
?
5km
WNW
ESE
B
0km
2km
4km
5km
WNW
ESE
C
0km
2km
4km
5km
Lower Cretaceous volcanic and sedimentary rocks
Neoarchean to Early Paleoproterozoic TTG, gneissic migmatite and granulite with meta-mafic or amphibolite lenses
Paleoproterozoic meta-sedimentary rocks
UHP gneiss
Late Jurassic biotite monzonitic granite
Early Cretaceous porphyritic granite
Early Cretaceous diorite and gabbro
Gneissic to mylonitic rocks
Ductile shearing
Brittle faulting
Sinistral strike slip fault

Figure 4.

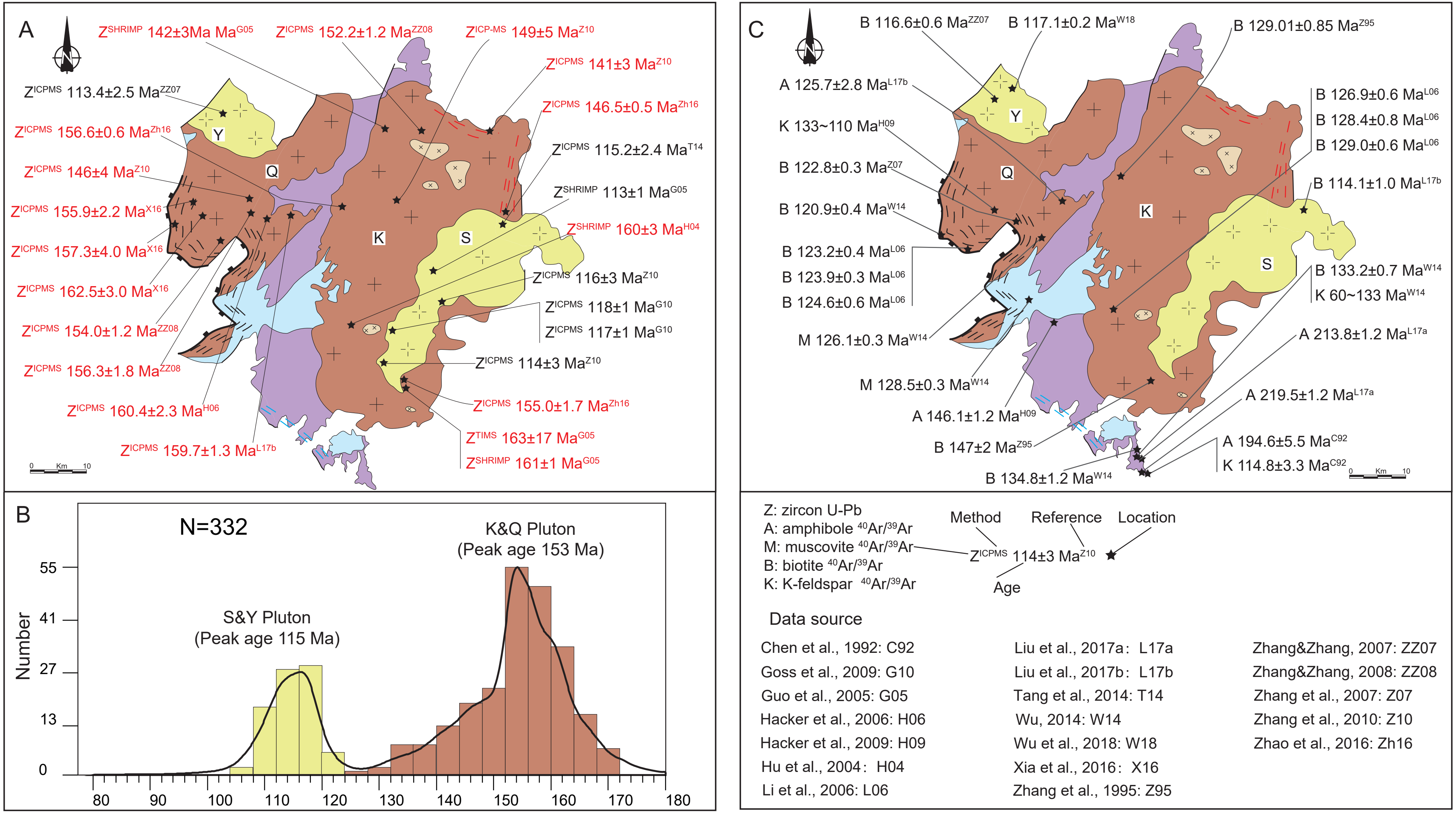
A
Z^{SHRIMP} 142±3Ma Ma^{G05}
Z^{ICPMS} 152.2±1.2 Ma^{ZZ08}
Z^{ICP-MS} 149±5 Ma^{Z10}
Z^{ICPMS} 141±3 Ma^{Z10}
Z^{ICPMS} 113.4±2.5 Ma^{ZZ07}
Z^{ICPMS} 146.5±0.5 Ma^{Zh16}
Z^{ICPMS} 156.6±0.6 Ma^{Zh16}
Z^{ICPMS} 115.2±2.4 Ma^{T14}
Z^{ICPMS} 146±4 Ma^{Z10}
Z^{SHRIMP} 113±1 Ma^{G05}
Z^{ICPMS} 155.9±2.2 Ma^{X16}
Z^{SHRIMP} 160±3 Ma^{H04}
Z^{ICPMS} 157.3±4.0 Ma^{X16}
Z^{ICPMS} 116±3 Ma^{Z10}
Z^{ICPMS} 162.5±3.0 Ma^{X16}
Z^{ICPMS} 118±1 Ma^{G10}
Z^{ICPMS} 117±1 Ma^{G10}
Z^{ICPMS} 154.0±1.2 Ma^{ZZ08}
Z^{ICPMS} 156.3±1.8 Ma^{ZZ08}
Z^{ICPMS} 114±3 Ma^{Z10}
Z^{ICPMS} 160.4±2.3 Ma^{H06}
Z^{ICPMS} 155.0±1.7 Ma^{Zh16}
Z^{TIMS} 163±17 Ma^{G05}
Z^{ICPMS} 159.7±1.3 Ma^{L17b}
Z^{SHRIMP} 161±1 Ma^{G05}
Y
Q
K
S
0 Km 10
B
N=332
K&Q Pluton
(Peak age 153 Ma)
S&Y Pluton
(Peak age 115 Ma)
Number
55
41
27
13
0
80
90
100
110
120
130
140
150
160
170
180
C
B 116.6±0.6 Ma^{ZZ07}
B 117.1±0.2 Ma^{W18}
B 129.01±0.85 Ma^{Z95}
A 125.7±2.8 Ma^{L17b}
B 126.9±0.6 Ma^{L06}
B 128.4±0.8 Ma^{L06}
K 133~110 Ma^{H09}
B 129.0±0.6 Ma^{L06}
B 122.8±0.3 Ma^{Z07}
B 114.1±1.0 Ma^{L17b}
B 120.9±0.4 Ma^{W14}
B 123.2±0.4 Ma^{L06}
B 123.9±0.3 Ma^{L06}
B 124.6±0.6 Ma^{L06}
B 133.2±0.7 Ma^{W14}
K 60~133 Ma^{W14}
M 126.1±0.3 Ma^{W14}
A 213.8±1.2 Ma^{L17a}
M 128.5±0.3 Ma^{W14}
A 219.5±1.2 Ma^{L17a}
A 146.1±1.2 Ma^{H09}
B 147±2 Ma^{Z95}
A 194.6±5.5 Ma^{C92}
K 114.8±3.3 Ma^{C92}
B 134.8±1.2 Ma^{W14}
0 Km 10
Z: zircon U-Pb
A: amphibole $^{40}Ar/^{39}Ar$
M: muscovite $^{40}Ar/^{39}Ar$
B: biotite $^{40}Ar/^{39}Ar$
K: K-feldspar $^{40}Ar/^{39}Ar$
Method
Reference
Location
Z^{ICPMS} 114±3 Ma^{Z10}
Age
Data source
Chen et al., 1992: C92
Goss et al., 2009: G10
Guo et al., 2005: G05
Hacker et al., 2006: H06
Hacker et al., 2009: H09
Hu et al., 2004: H04
Li et al., 2006: L06
Liu et al., 2017a: L17a
Liu et al., 2017b: L17b
Tang et al., 2014: T14
Wu, 2014: W14
Wu et al., 2018: W18
Xia et al., 2016: X16
Zhang et al., 1995: Z95
Zhang&Zhang, 2007: ZZ07
Zhang&Zhang, 2008: ZZ08
Zhang et al., 2007: Z07
Zhang et al., 2010: Z10
Zhao et al., 2016: Zh16

Figure 5.

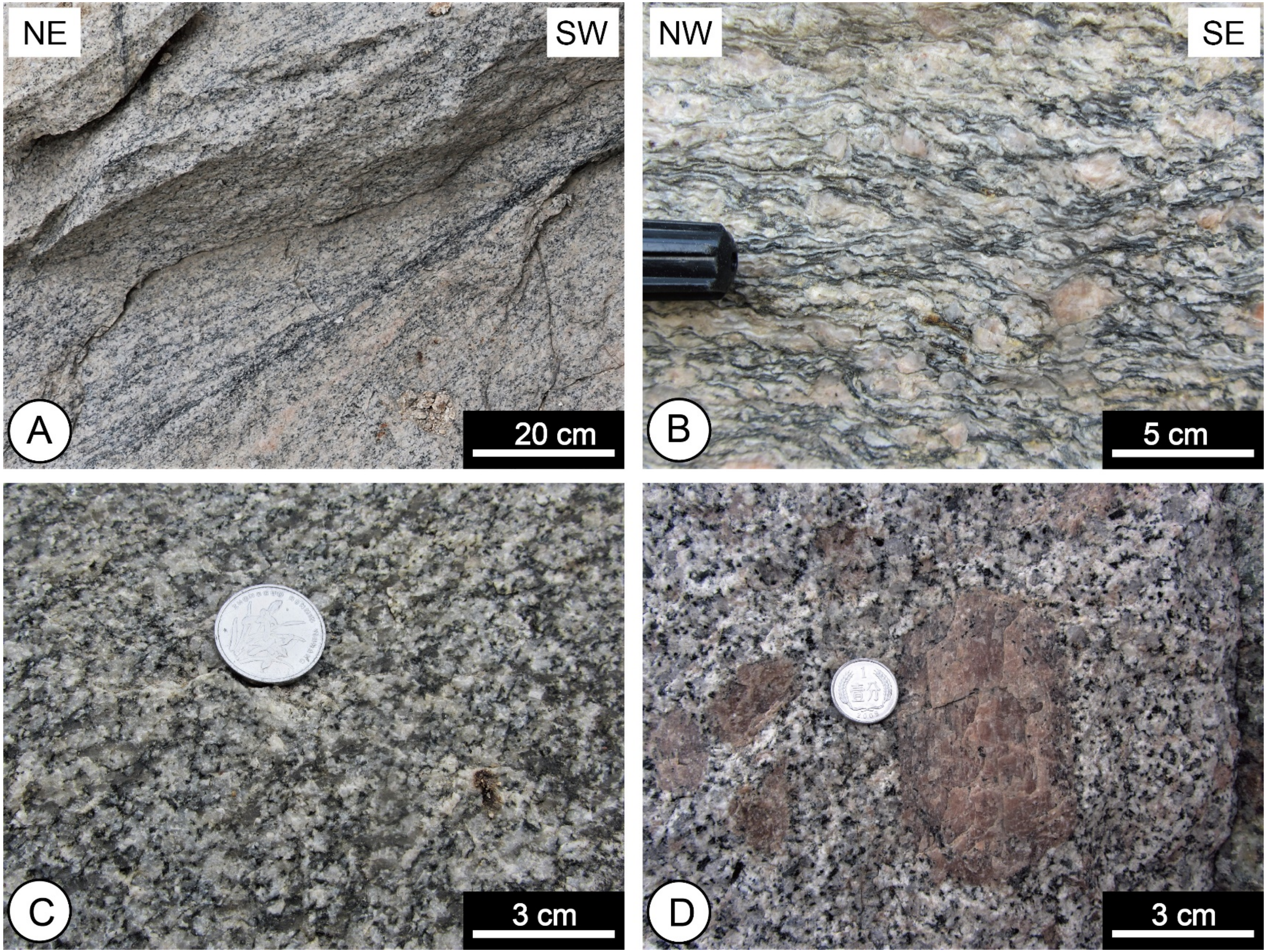
NE
SW
A
20 cm
NW
SE
B
5 cm
C
3 cm
D
3 cm

Figure 6.

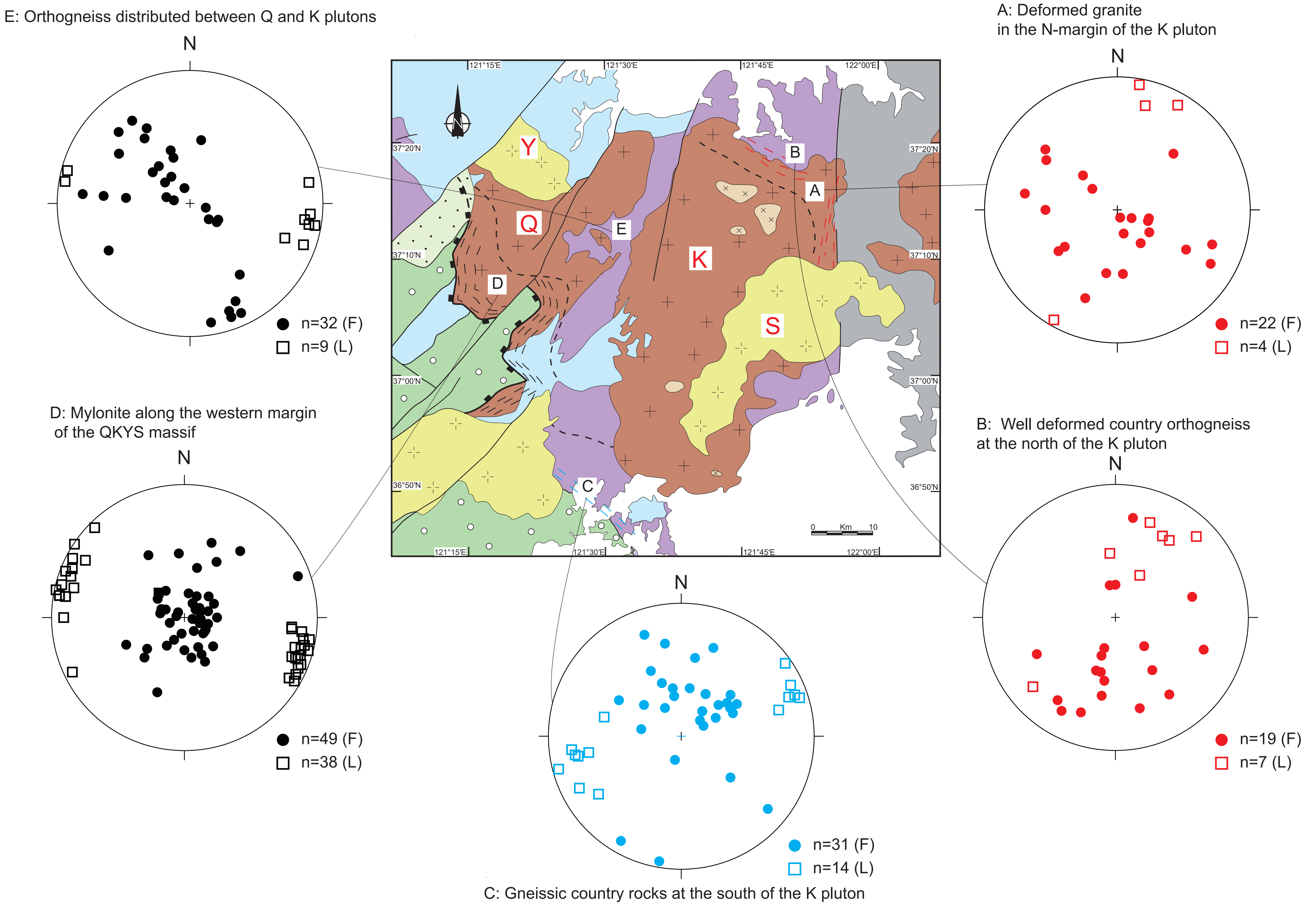

E: Orthogneiss distributed between Q and K plutons
N
n=32 (F)
n=9 (L)
A: Deformed granite
in the N-margin of the K pluton
N
n=22 (F)
n=4 (L)
121°15'E
121°30'E
121°45'E
122°00'E
37°20'N
37°10'N
37°00'N
36°50'N
Y
Q
K
S
A
B
C
D
E
0 Km 10
D: Mylonite along the western margin
of the QKYS massif
N
n=49 (F)
n=38 (L)
B: Well deformed country orthogneiss
at the north of the K pluton
N
n=19 (F)
n=7 (L)
N
n=31 (F)
n=14 (L)
C: Gneissic country rocks at the south of the K pluton

Figure 7.

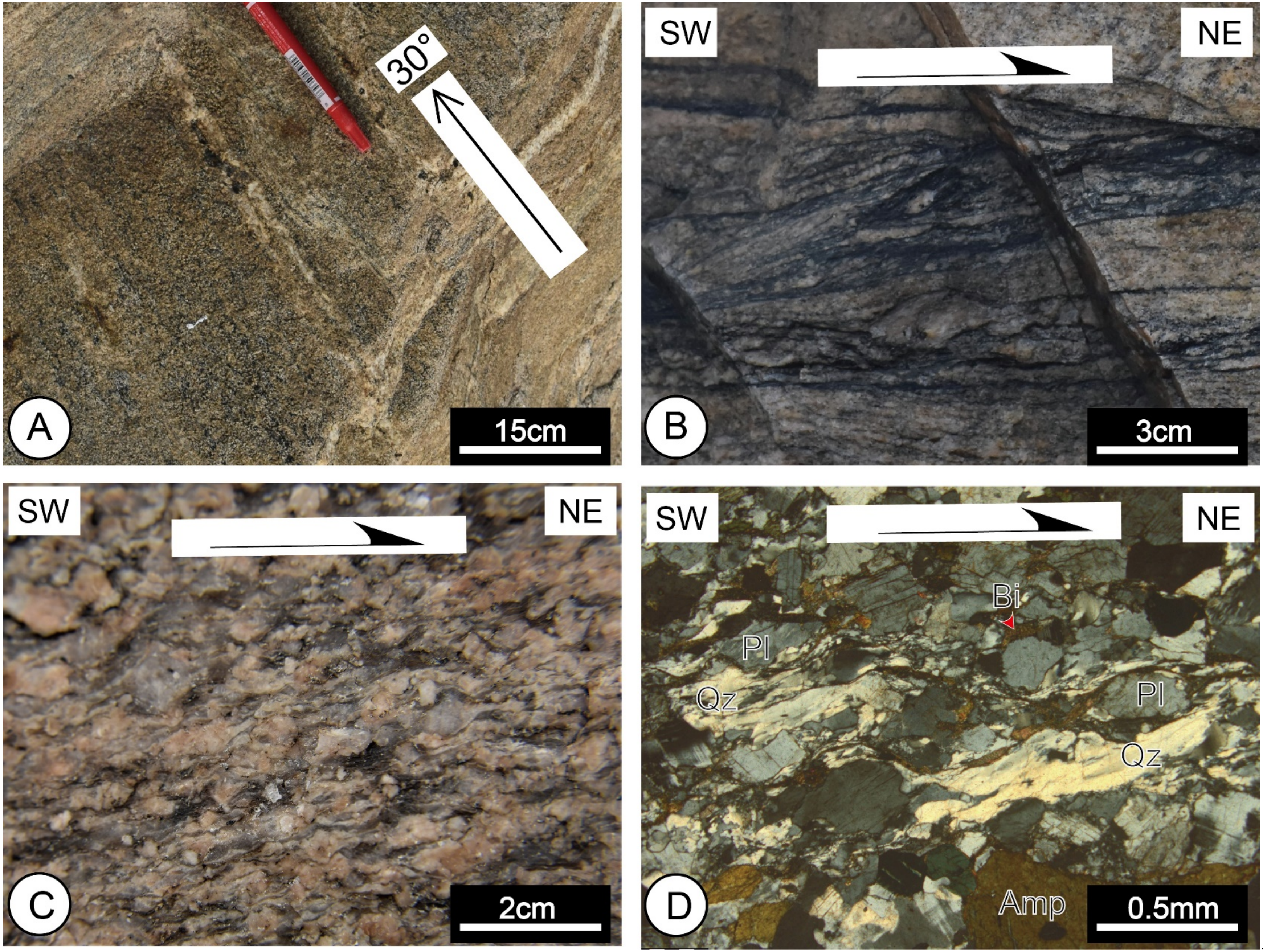

30°
15cm
A
SW
NE
3cm
B
SW
NE
2cm
C
SW
NE
Bi
Pl
Qz
Pl
Qz
Amp
0.5mm
D

Figure 8.

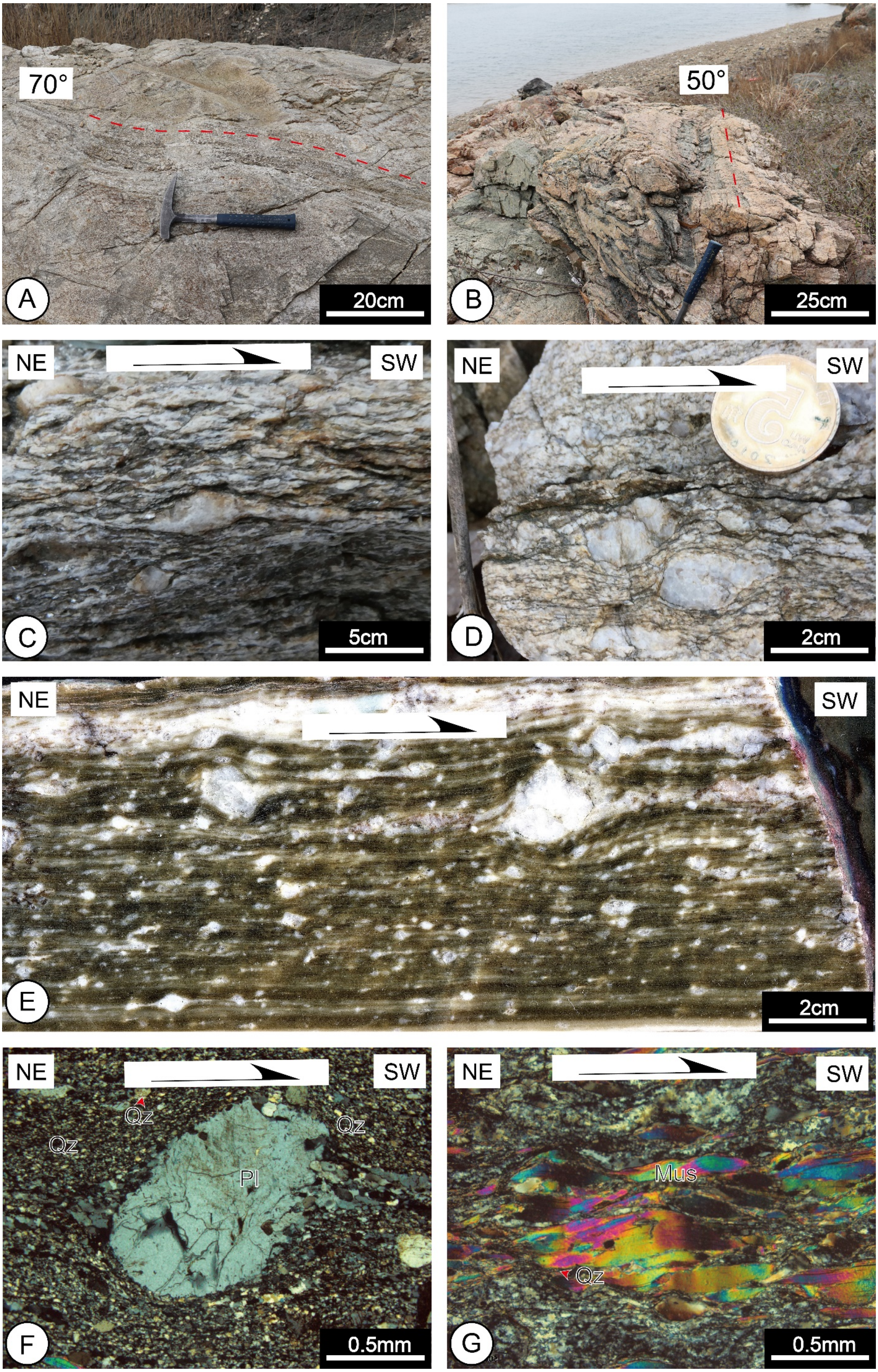

70°
A
20cm
50°
B
25cm
NE
SW
C
5cm
NE
SW
D
2cm
NE
SW
E
2cm
NE
SW
Qz
Qz
Qz
Pl
F
0.5mm
NE
SW
Mus
Qz
G
0.5mm

Figure 9.

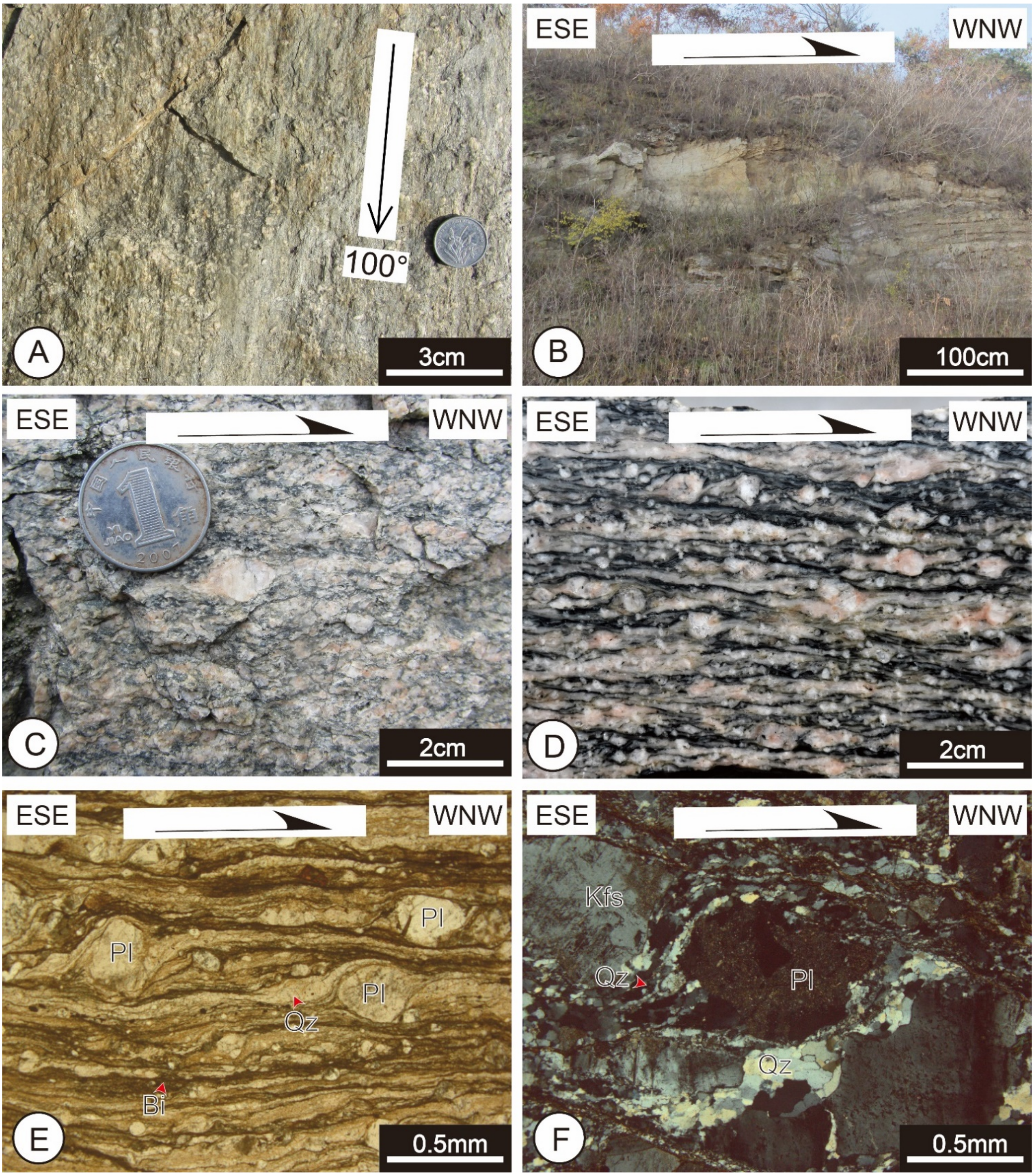

A
100°
3cm
ESE
WNW
B
100cm
ESE
WNW
C
2cm
ESE
WNW
D
2cm
ESE
WNW
Pl
Pl
Pl
Qz
Bi
E
0.5mm
ESE
WNW
Kfs
Qz
Pl
Qz
F
0.5mm

Figure 10.

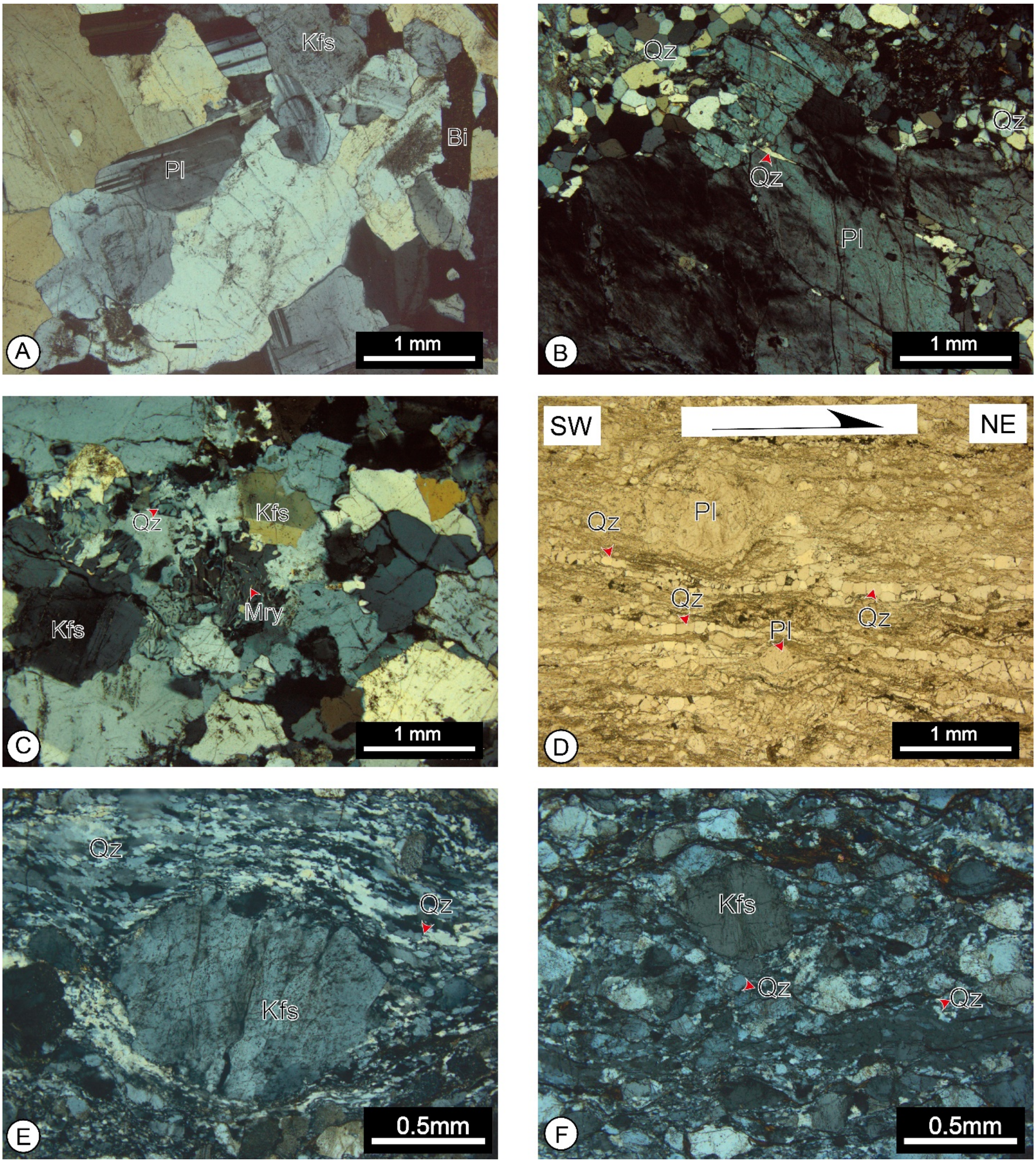
Kfs
Bi
Pl
A
1 mm
Qz
Qz
Qz
Pl
B
1 mm
Qz
Kfs
Mry
Kfs
C
1 mm
SW
NE
Qz
Pl
Qz
Qz
Pl
D
1 mm
Qz
Qz
Kfs
E
0.5mm
Kfs
Qz
Qz
F
0.5mm

Figure 11.

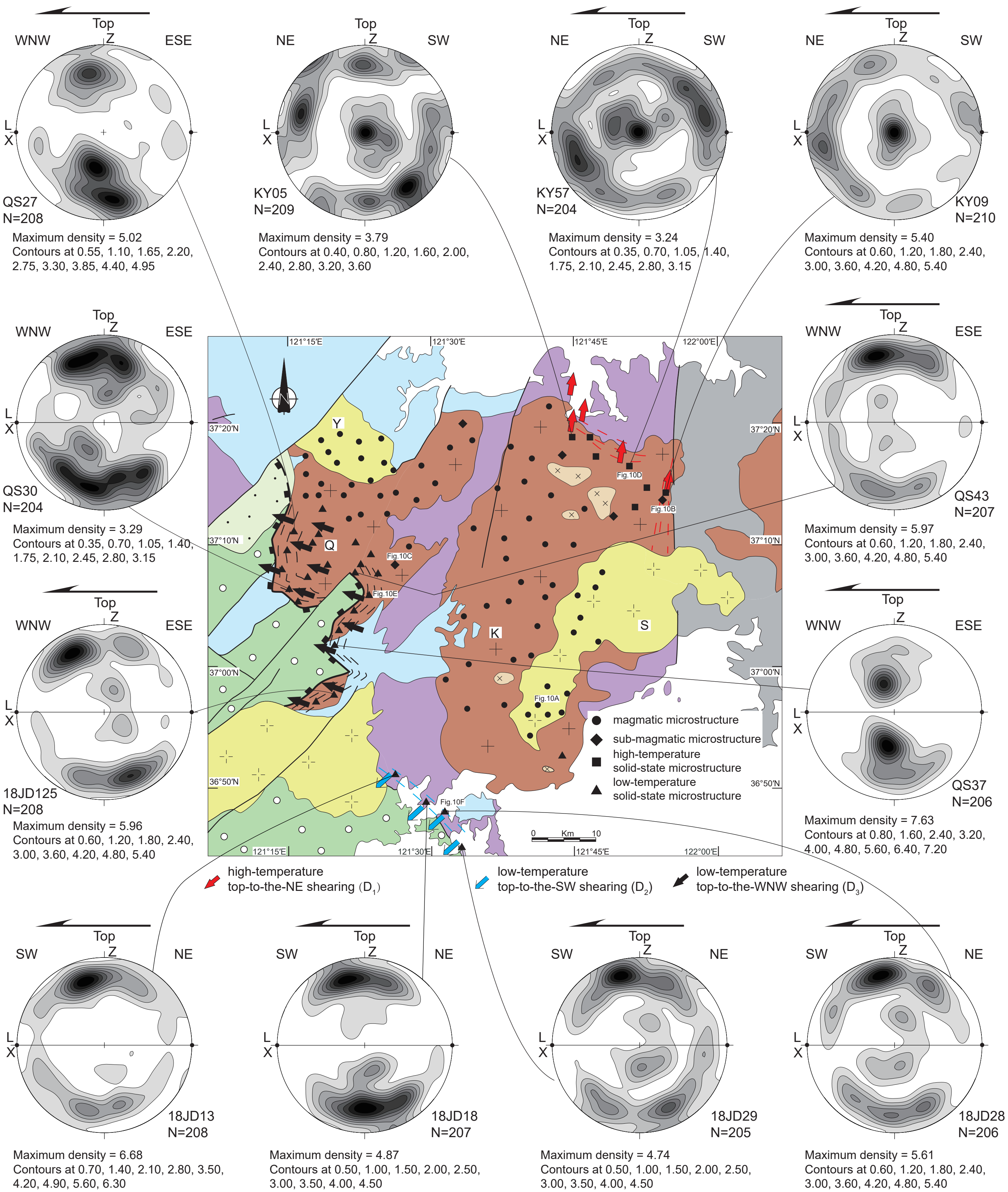

Top
WNW
ESE
Z
L
X
QS27
N=208
Maximum density = 5.02
Contours at 0.55, 1.10, 1.65, 2.20, 2.75, 3.30, 3.85, 4.40, 4.95
NE
SW
KY05
N=209
Maximum density = 3.79
Contours at 0.40, 0.80, 1.20, 1.60, 2.00, 2.40, 2.80, 3.20, 3.60
KY57
N=204
Maximum density = 3.24
Contours at 0.35, 0.70, 1.05, 1.40, 1.75, 2.10, 2.45, 2.80, 3.15
KY09
N=210
Maximum density = 5.40
Contours at 0.60, 1.20, 1.80, 2.40, 3.00, 3.60, 4.20, 4.80, 5.40
QS30
N=204
Maximum density = 3.29
Contours at 0.35, 0.70, 1.05, 1.40, 1.75, 2.10, 2.45, 2.80, 3.15
QS43
N=207
Maximum density = 5.97
Contours at 0.60, 1.20, 1.80, 2.40, 3.00, 3.60, 4.20, 4.80, 5.40
18JD125
N=208
Maximum density = 5.96
Contours at 0.60, 1.20, 1.80, 2.40, 3.00, 3.60, 4.20, 4.80, 5.40
QS37
N=206
Maximum density = 7.63
Contours at 0.80, 1.60, 2.40, 3.20, 4.00, 4.80, 5.60, 6.40, 7.20
121°15′E
121°30′E
121°45′E
122°00′E
37°20′N
37°10′N
37°00′N
36°50′N
Y
Q
K
S
Fig.10A
Fig.10B
Fig.10C
Fig.10D
Fig.10E
Fig.10F
0 Km 10
magmatic microstructure
sub-magmatic microstructure
high-temperature solid-state microstructure
low-temperature solid-state microstructure
high-temperature top-to-the-NE shearing (D1)
low-temperature top-to-the-SW shearing (D2)
low-temperature top-to-the-WNW shearing (D3)
18JD13
N=208
Maximum density = 6.68
Contours at 0.70, 1.40, 2.10, 2.80, 3.50, 4.20, 4.90, 5.60, 6.30
18JD18
N=207
Maximum density = 4.87
Contours at 0.50, 1.00, 1.50, 2.00, 2.50, 3.00, 3.50, 4.00, 4.50
18JD29
N=205
Maximum density = 4.74
Contours at 0.50, 1.00, 1.50, 2.00, 2.50, 3.00, 3.50, 4.00, 4.50
18JD28
N=206
Maximum density = 5.61
Contours at 0.60, 1.20, 1.80, 2.40, 3.00, 3.60, 4.20, 4.80, 5.40

Figure 12.

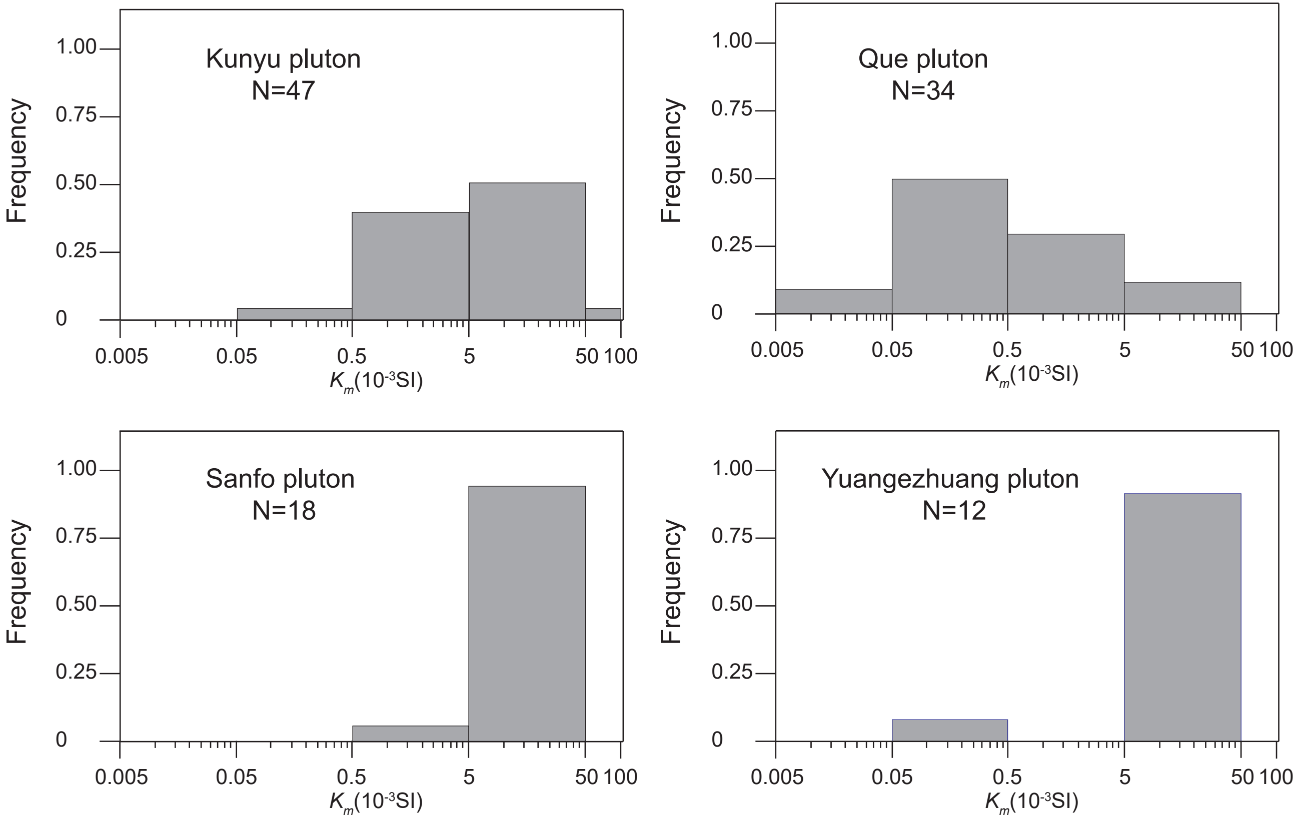

Kunyu pluton
N=47
Que pluton
N=34
Sanfo pluton
N=18
Yuangezhuang pluton
N=12
Frequency
1.00
0.75
0.50
0.25
0
0.005
0.05
0.5
5
50 100
K_m(10^{-3}SI)

Figure 13.

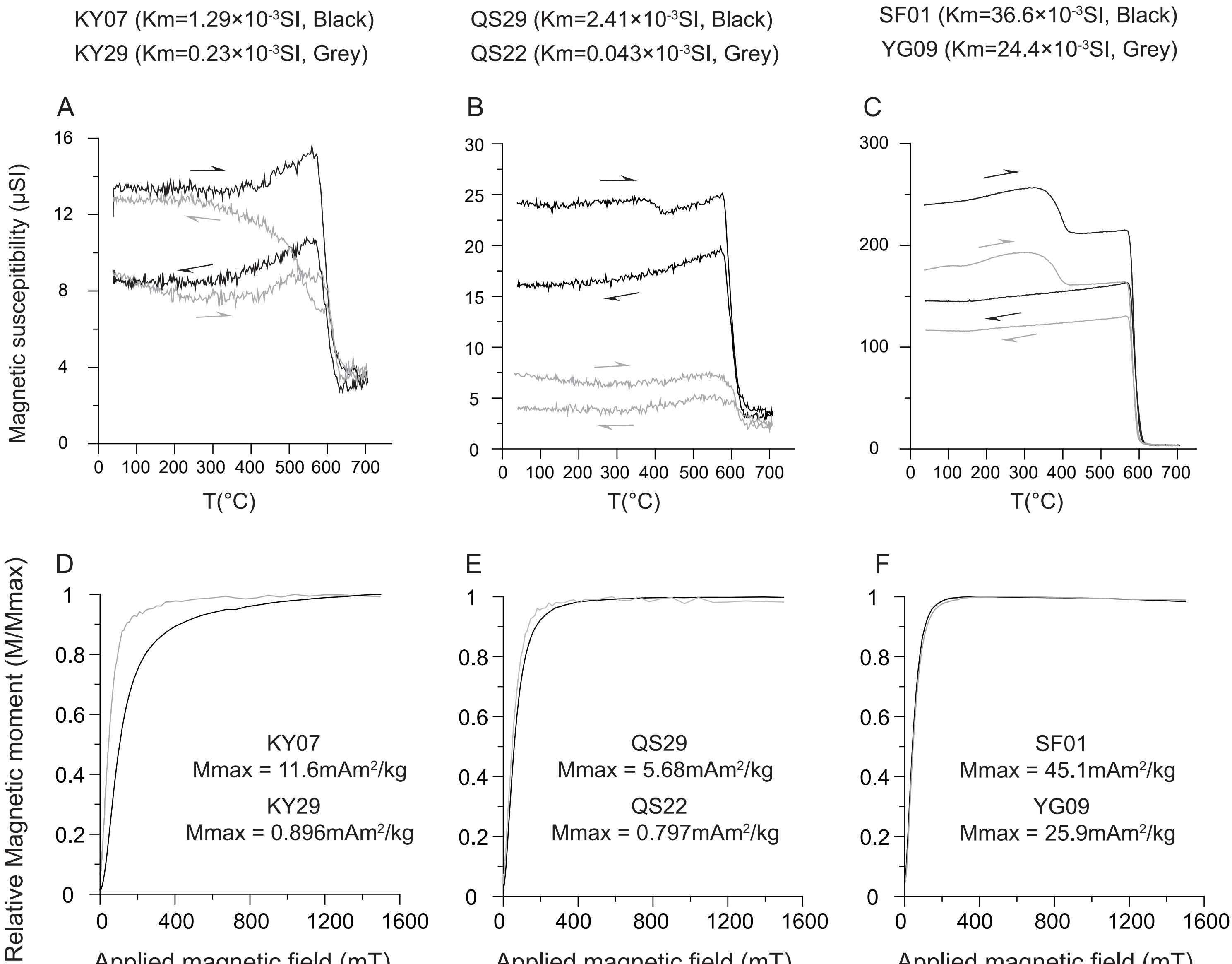
KY07 (Km=1.29×10-3SI, Black)
KY29 (Km=0.23×10-3SI, Grey)
QS29 (Km=2.41×10-3SI, Black)
QS22 (Km=0.043×10-3SI, Grey)
SF01 (Km=36.6×10-3SI, Black)
YG09 (Km=24.4×10-3SI, Grey)
A
B
C
Magnetic susceptibility (μSI)
T(°C)
D
E
F
Relative Magnetic moment (M/Mmax)
Applied magnetic field (mT)
KY07
Mmax = 11.6mAm2/kg
KY29
Mmax = 0.896mAm2/kg
QS29
Mmax = 5.68mAm2/kg
QS22
Mmax = 0.797mAm2/kg
SF01
Mmax = 45.1mAm2/kg
YG09
Mmax = 25.9mAm2/kg

Figure 14.

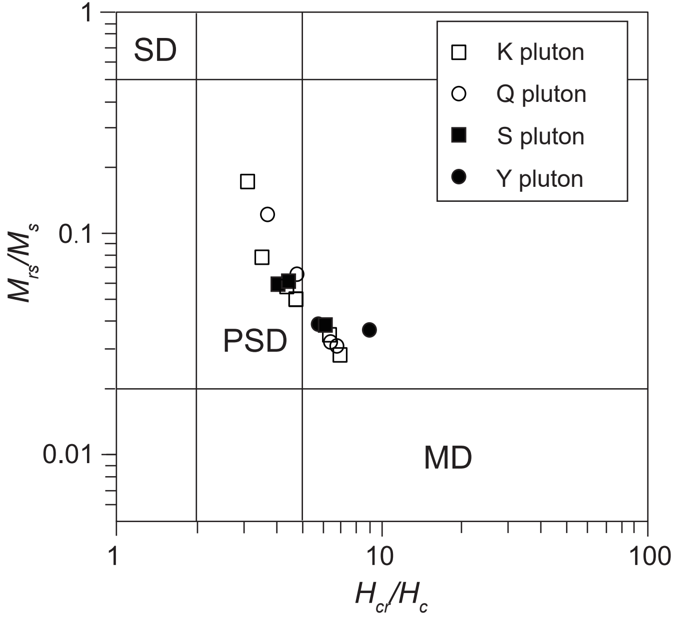

SD
PSD
MD
K pluton
Q pluton
S pluton
Y pluton
1
0.1
0.01
1
10
100
M_{rs}/M_s
H_{cr}/H_c

Figure 15.

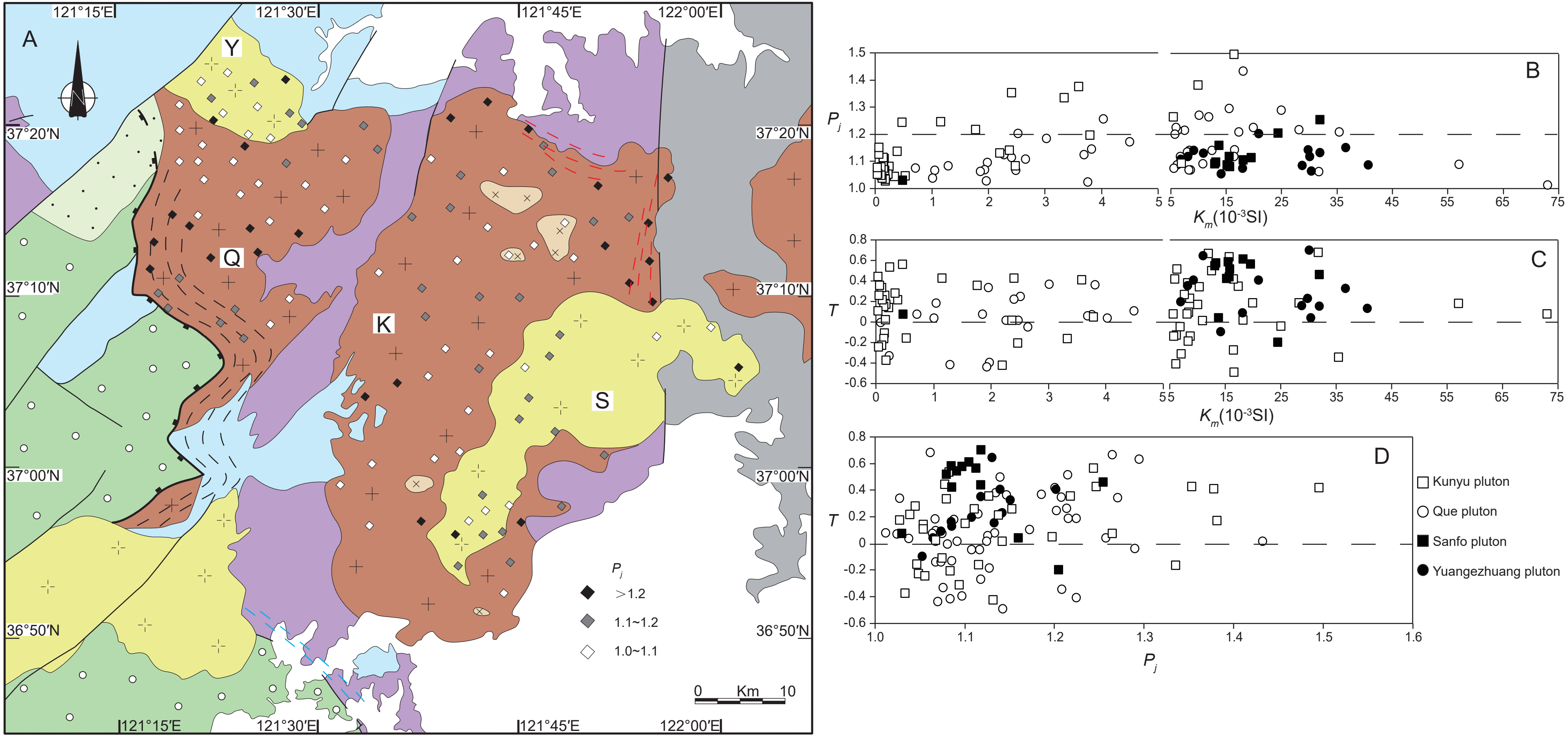

A
B
C
D
Y
Q
K
S
121°15′E
121°30′E
121°45′E
122°00′E
37°20′N
37°10′N
37°00′N
36°50′N
P_j
>1.2
1.1~1.2
1.0~1.1
0 Km 10
$K_m(10^{-3}SI)$
T
Kunyu pluton
Que pluton
Sanfo pluton
Yuangezhuang pluton

Figure 16.

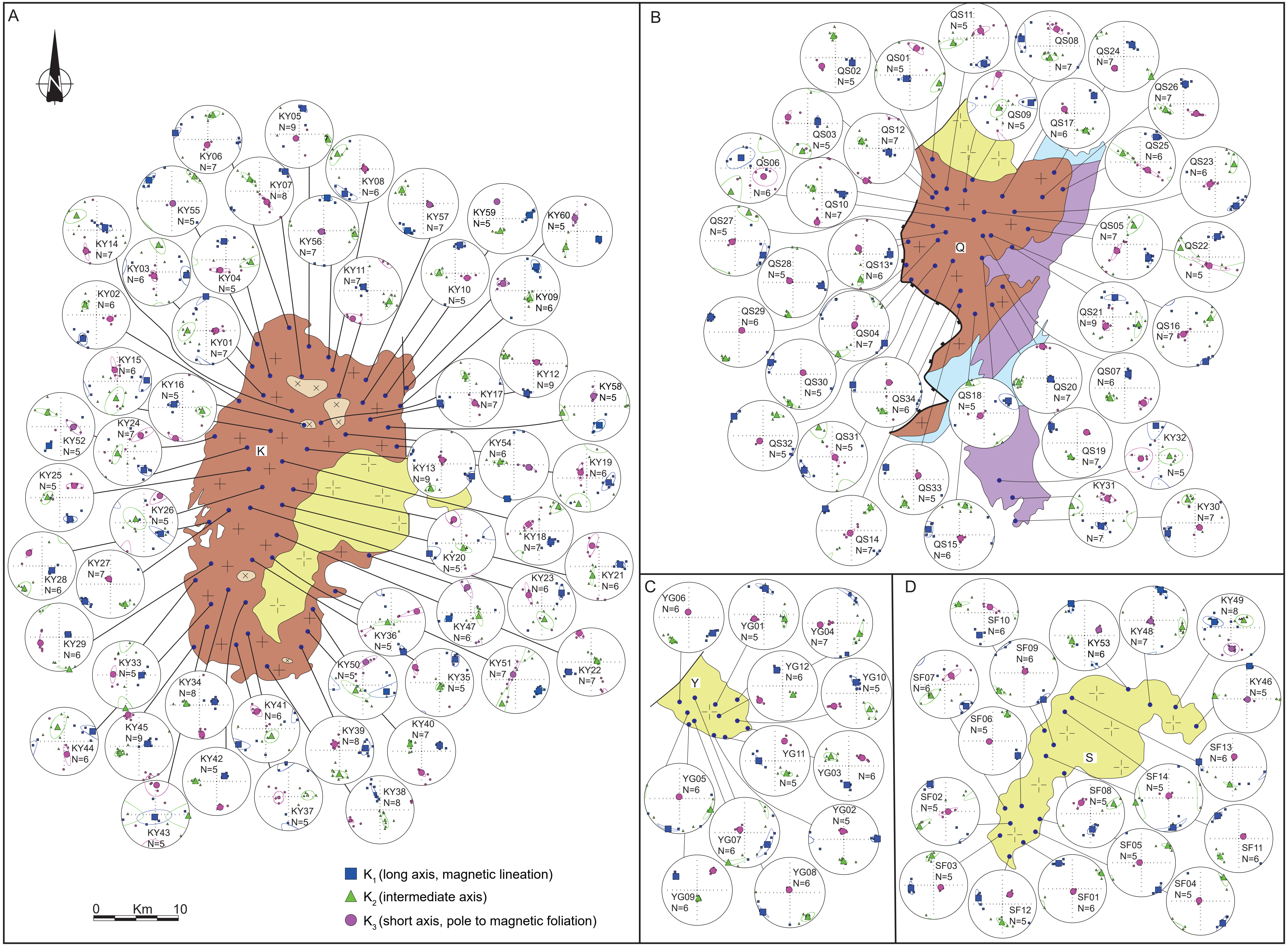

A
B
C
D
K
Q
Y
S
0 Km 10
K1 (long axis, magnetic lineation)
K2 (intermediate axis)
K3 (short axis, pole to magnetic foliation)

Figure 17.

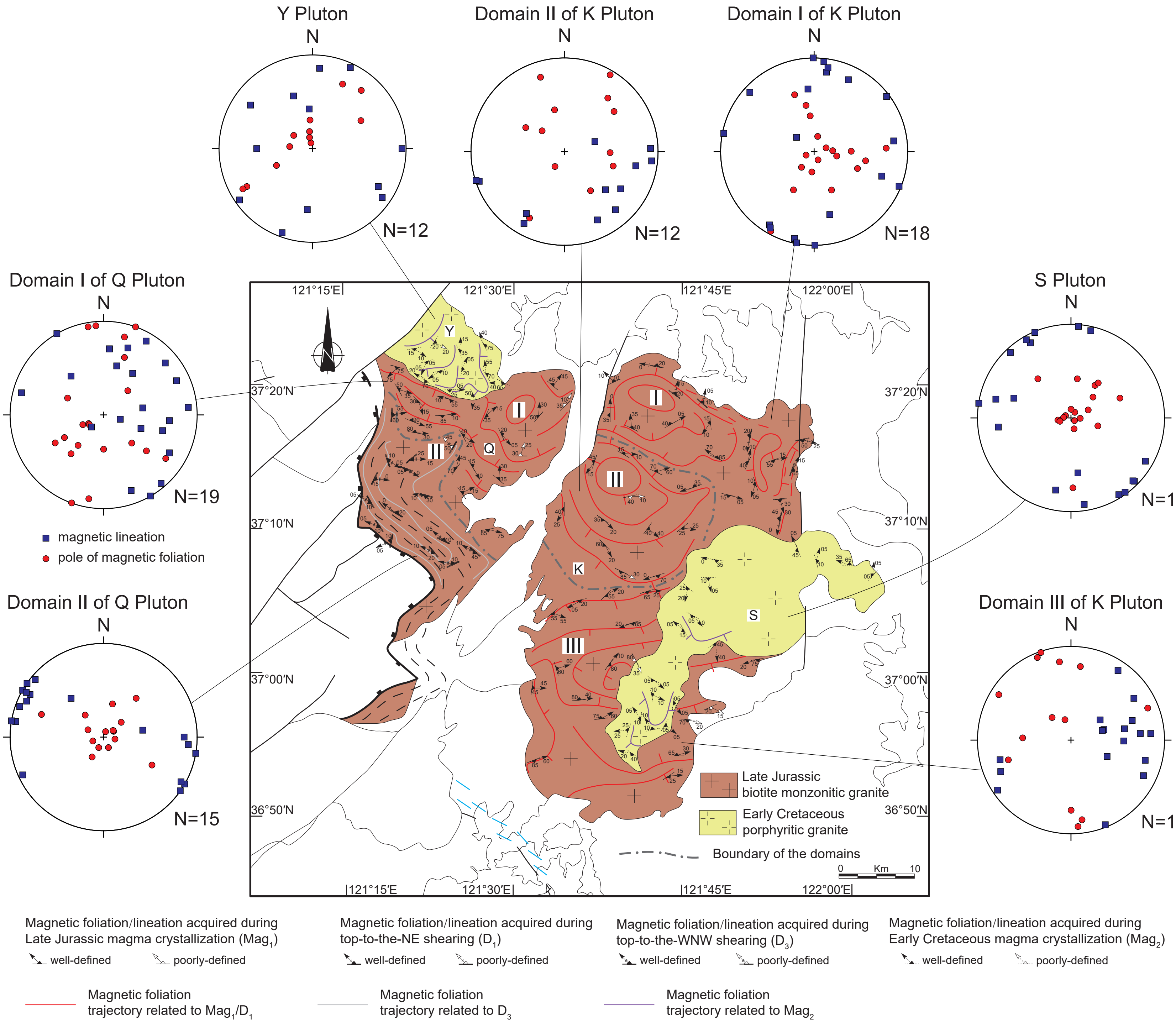

Y Pluton
N
N=12
Domain II of K Pluton
N
N=12
Domain I of K Pluton
N
N=18
Domain I of Q Pluton
N
N=19
magnetic lineation
pole of magnetic foliation
Domain II of Q Pluton
N
N=15
S Pluton
N
N=18
Domain III of K Pluton
N
N=17
121°15′E
121°30′E
121°45′E
122°00′E
37°20′N
37°10′N
37°00′N
36°50′N
Y
Q
K
S
I
II
III
Late Jurassic biotite monzonitic granite
Early Cretaceous porphyritic granite
Boundary of the domains
0 Km 10
Magnetic foliation/lineation acquired during Late Jurassic magma crystallization (Mag1)
well-defined
poorly-defined
Magnetic foliation/lineation acquired during top-to-the-NE shearing (D1)
well-defined
poorly-defined
Magnetic foliation/lineation acquired during top-to-the-WNW shearing (D3)
well-defined
poorly-defined
Magnetic foliation/lineation acquired during Early Cretaceous magma crystallization (Mag2)
well-defined
poorly-defined
Magnetic foliation trajectory related to Mag1/D1
Magnetic foliation trajectory related to D3
Magnetic foliation trajectory related to Mag2

Figure 18.

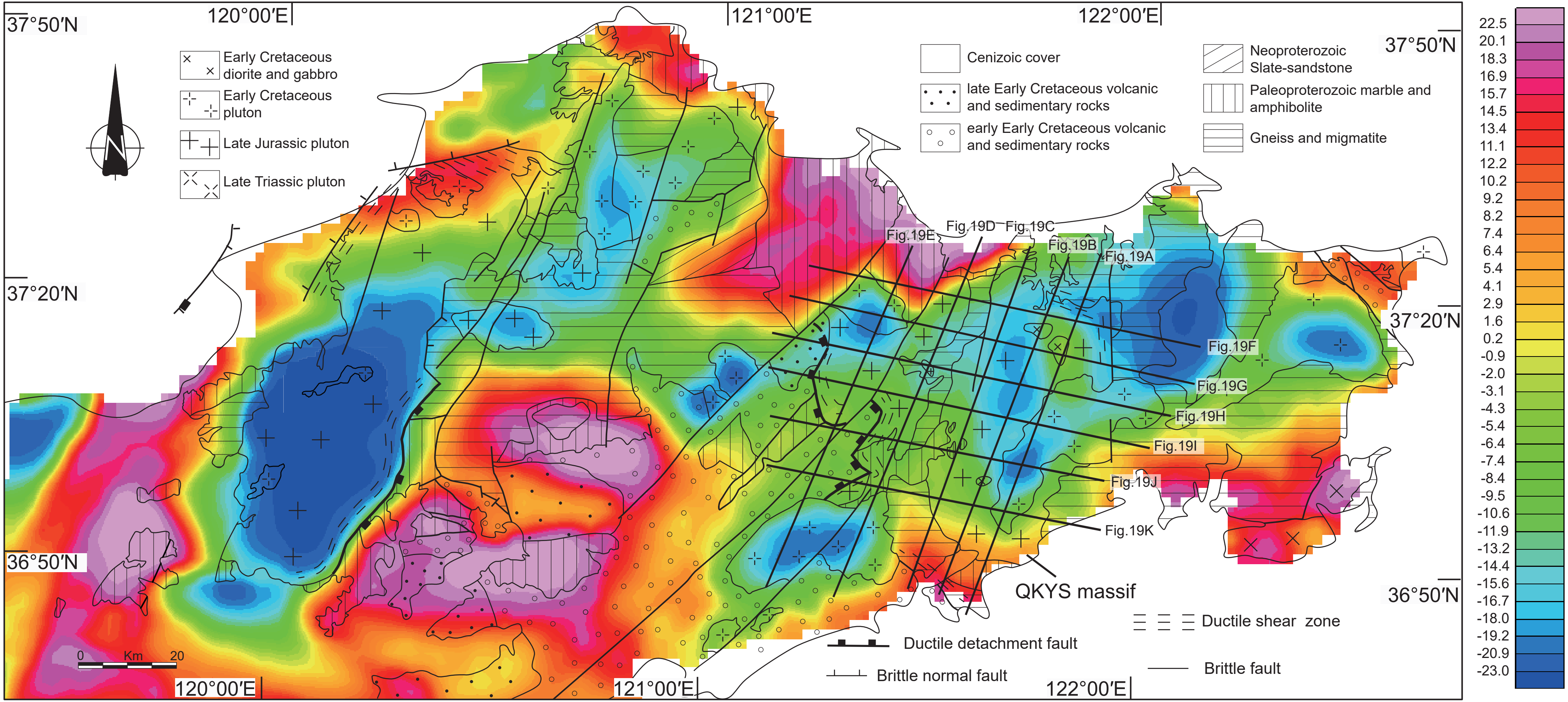

37°50′N
120°00′E
121°00′E
122°00′E
37°50′N
Early Cretaceous diorite and gabbro
Early Cretaceous pluton
Late Jurassic pluton
Late Triassic pluton
Cenizoic cover
late Early Cretaceous volcanic and sedimentary rocks
early Early Cretaceous volcanic and sedimentary rocks
Neoproterozoic Slate-sandstone
Paleoproterozoic marble and amphibolite
Gneiss and migmatite
37°20′N
37°20′N
36°50′N
36°50′N
Fig.19A
Fig.19B
Fig.19C
Fig.19D
Fig.19E
Fig.19F
Fig.19G
Fig.19H
Fig.19I
Fig.19J
Fig.19K
QKYS massif
0 Km 20
120°00′E
121°00′E
122°00′E
Ductile shear zone
Ductile detachment fault
Brittle normal fault
Brittle fault
22.5
20.1
18.3
16.9
15.7
14.5
13.4
11.1
12.2
10.2
9.2
8.2
7.4
6.4
5.4
4.1
2.9
1.6
0.2
-0.9
-2.0
-3.1
-4.3
-5.4
-6.4
-7.4
-8.4
-9.5
-10.6
-11.9
-13.2
-14.4
-15.6
-16.7
-18.0
-19.2
-20.9
-23.0

Figure 19.

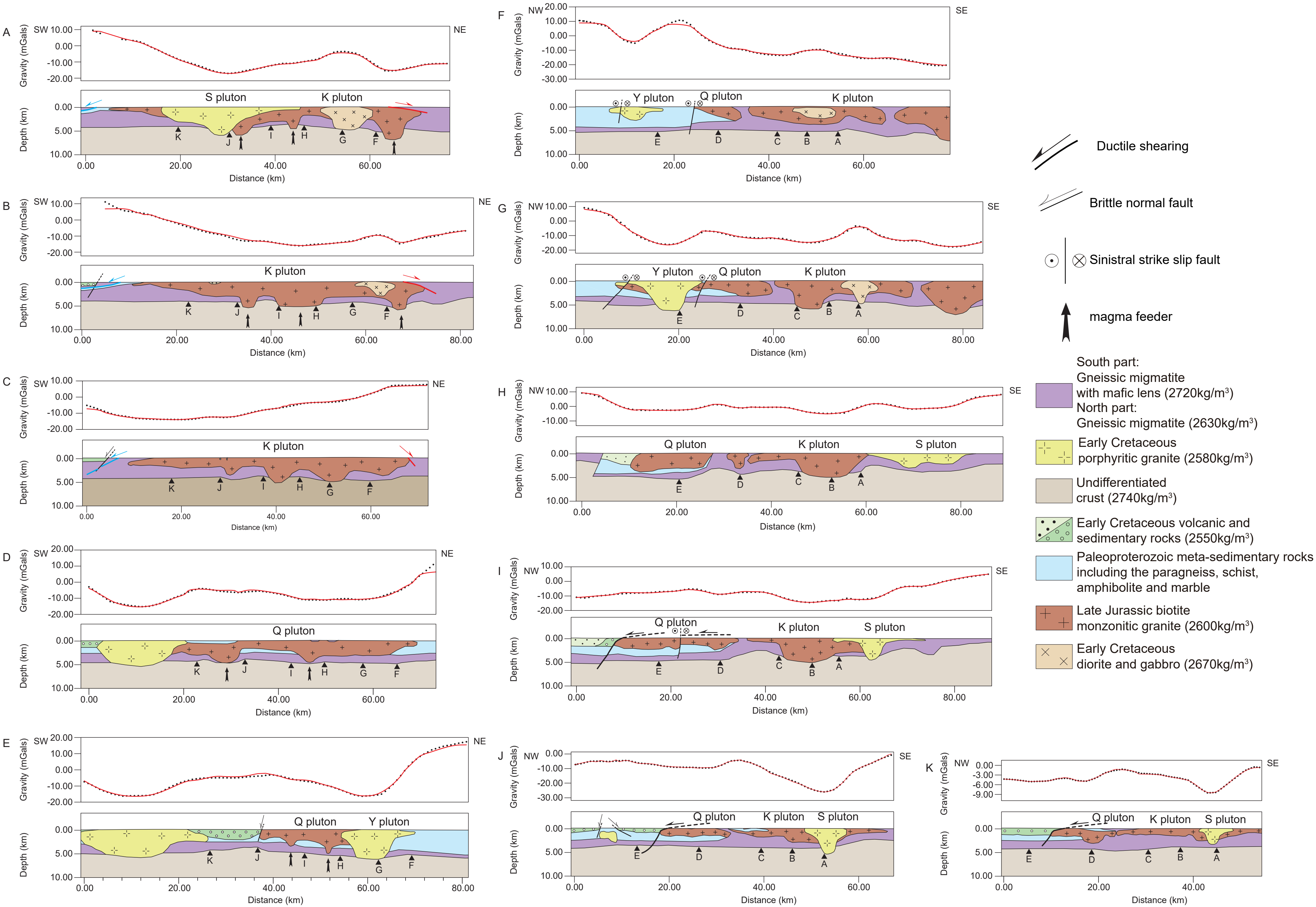

A
SW
NE
S pluton
K pluton
B
K pluton
C
K pluton
D
Q pluton
E
Q pluton
Y pluton
F
NW
SE
Y pluton
Q pluton
K pluton
G
Y pluton
Q pluton
K pluton
H
Q pluton
K pluton
S pluton
I
Q pluton
K pluton
S pluton
J
Q pluton
K pluton
S pluton
K
Q pluton
K pluton
S pluton
Gravity (mGals)
Depth (km)
Distance (km)
Ductile shearing
Brittle normal fault
Sinistral strike slip fault
magma feeder
South part:
Gneissic migmatite
with mafic lens (2720kg/m³)
North part:
Gneissic migmatite (2630kg/m³)
Early Cretaceous
porphyritic granite (2580kg/m³)
Undifferentiated
crust (2740kg/m³)
Early Cretaceous volcanic and
sedimentary rocks (2550kg/m³)
Paleoproterozoic meta-sedimentary rocks
including the paragneiss, schist,
amphibolite and marble
Late Jurassic biotite
monzonitic granite (2600kg/m³)
Early Cretaceous
diorite and gabbro (2670kg/m³)

Figure 20.

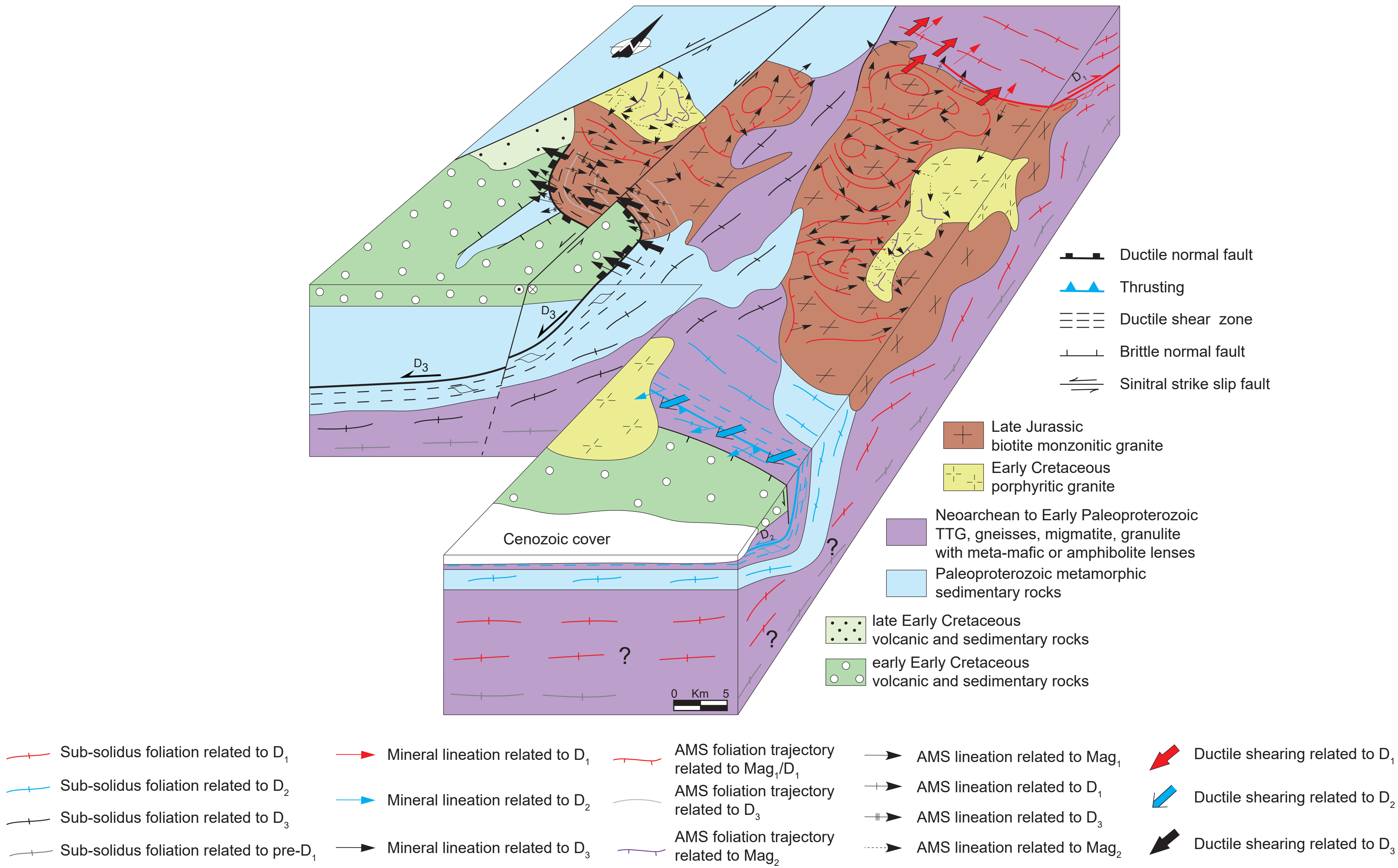
D3
D3
D1
D2
Cenozoic cover
?
?
?
0 Km 5
Ductile normal fault
Thrusting
Ductile shear zone
Brittle normal fault
Sinitral strike slip fault
Late Jurassic biotite monzonitic granite
Early Cretaceous porphyritic granite
Neoarchean to Early Paleoproterozoic TTG, gneisses, migmatite, granulite with meta-mafic or amphibolite lenses
Paleoproterozoic metamorphic sedimentary rocks
late Early Cretaceous volcanic and sedimentary rocks
early Early Cretaceous volcanic and sedimentary rocks
Sub-solidus foliation related to D_1
Sub-solidus foliation related to D_2
Sub-solidus foliation related to D_3
Sub-solidus foliation related to pre-D_1
Mineral lineation related to D_1
Mineral lineation related to D_2
Mineral lineation related to D_3
AMS foliation trajectory related to Mag_1/D_1
AMS foliation trajectory related to D_3
AMS foliation trajectory related to Mag_2
AMS lineation related to Mag_1
AMS lineation related to D_1
AMS lineation related to D_3
AMS lineation related to Mag_2
Ductile shearing related to D_1
Ductile shearing related to D_2
Ductile shearing related to D_3

Figure 21.

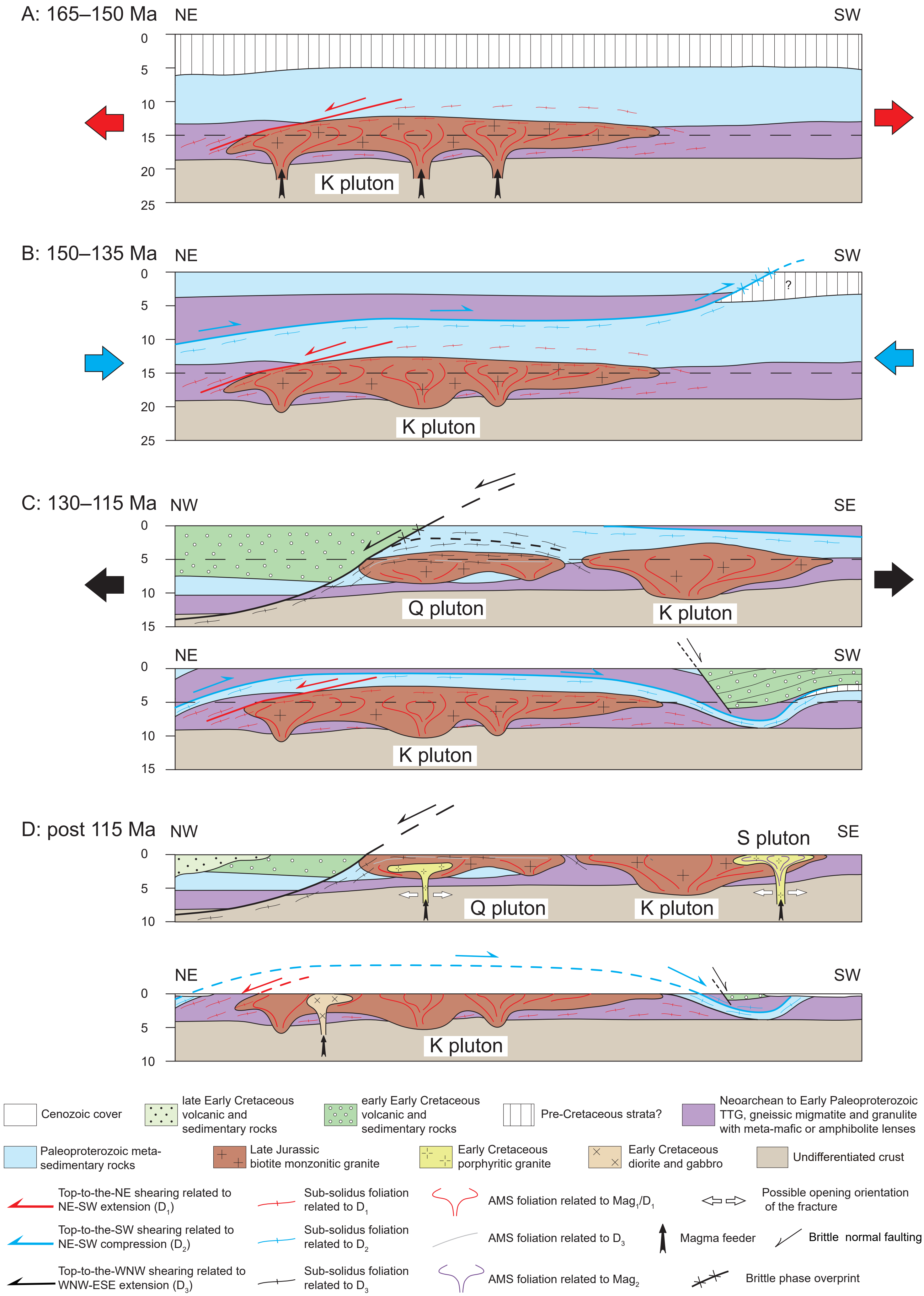

A: 165–150 Ma
NE
SW
0
5
10
15
20
25
K pluton
B: 150–135 Ma
NE
SW
?
K pluton
C: 130–115 Ma
NW
SE
Q pluton
K pluton
NE
SW
K pluton
D: post 115 Ma
NW
SE
S pluton
Q pluton
K pluton
NE
SW
K pluton
Cenozoic cover
late Early Cretaceous volcanic and sedimentary rocks
early Early Cretaceous volcanic and sedimentary rocks
Pre-Cretaceous strata?
Neoarchean to Early Paleoproterozoic TTG, gneissic migmatite and granulite with meta-mafic or amphibolite lenses
Paleoproterozoic meta-sedimentary rocks
Late Jurassic biotite monzonitic granite
Early Cretaceous porphyritic granite
Early Cretaceous diorite and gabbro
Undifferentiated crust
Top-to-the-NE shearing related to NE-SW extension (D_1)
Sub-solidus foliation related to D_1
AMS foliation related to Mag_1/D_1
Possible opening orientation of the fracture
Top-to-the-SW shearing related to NE-SW compression (D_2)
Sub-solidus foliation related to D_2
AMS foliation related to D_3
Magma feeder
Brittle normal faulting
Top-to-the-WNW shearing related to WNW-ESE extension (D_3)
Sub-solidus foliation related to D_3
AMS foliation related to Mag_2
Brittle phase overprint

Figure 22.

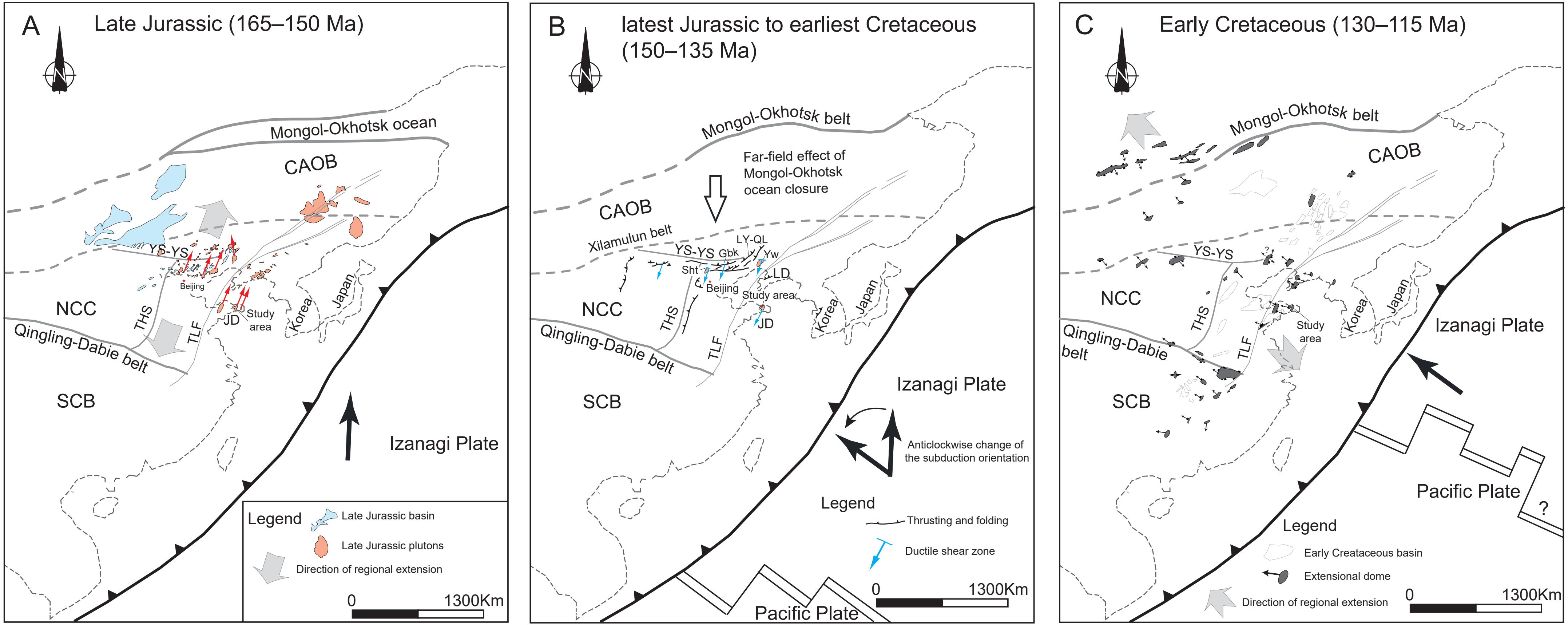

A
Late Jurassic (165–150 Ma)
Mongol-Okhotsk ocean
CAOB
YS-YS
Beijing
NCC
THS
TLF
JD
Study area
Korea
Japan
Qingling-Dabie belt
SCB
Izanagi Plate
Legend
Late Jurassic basin
Late Jurassic plutons
Direction of regional extension
0
1300Km
B
latest Jurassic to earliest Cretaceous (150–135 Ma)
Mongol-Okhotsk belt
Far-field effect of Mongol-Okhotsk ocean closure
CAOB
Xilamulun belt
LY-QL
YS-YS
Gbk
Yw
Sht
LD
Beijing
Study area
JD
NCC
THS
TLF
Korea
Japan
Qingling-Dabie belt
SCB
Izanagi Plate
Anticlockwise change of the subduction orientation
Legend
Thrusting and folding
Ductile shear zone
0
1300Km
Pacific Plate
C
Early Cretaceous (130–115 Ma)
Mongol-Okhotsk belt
CAOB
YS-YS
NCC
THS
TLF
Study area
Korea
Japan
Izanagi Plate
Qingling-Dabie belt
SCB
Pacific Plate
?
Legend
Early Createaceous basin
Extensional dome
Direction of regional extension
0
1300Km